



Electroosmotic mixing of viscoplastic fluids in a microchannel

Sumit Kumar Mehta ¹ and Pranab Kumar Mondal ^{1,2,*}¹*Microfluidics and Microscale Transport Processes Laboratory, Department of Mechanical Engineering, Indian Institute of Technology Guwahati, Guwahati-781039, Assam, India*²*School of Agro and Rural Technology, Indian Institute of Technology Guwahati, Guwahati-781039, Assam, India*

(Received 5 April 2023; accepted 2 January 2024; published 5 February 2024)

Viscoplastic fluids flow through a microfluidic channel having a built-in two-part cylinder inside, while the upstream and downstream parts of the cylinder bear the surface potential of the same sign but of different magnitudes. We consider the Herschel-Bulkley model in describing the rheology of the viscoplastic fluids considered in this analysis. Consistent with the finite element method, the modeling framework employed here considers the prevailing effect of fluid rheology, and geometrical configuration—modulated electroosmotic forcing while solving the transport equations governing the mixing dynamics. We demonstrate that electroosmotic forcing, induced from the topology-modulated electrical double-layer effect, upon interacting with the prevalent viscous force in the field, leads to the flow reversal in the region closer to the built-in cylinder, which in turn, gives rise to the formation of vortices therein. As seen, the shear-thinning nature of the viscoplastic fluid results in an enhancement of the recirculation velocity strength, albeit the inevitable yield stress of the fluid sparsely influences the onset of flow recirculation. By showing the impact of the geometrical parameter of the cylinder and viscoplastic effect (signifying the effect of yield stress) on the recirculation strength, we show that the developed vortices in the pathway promote mixing of the constituent fluids nontrivially. Also, the characteristic time for shear-induced binary aggregation that illustrates the underlying mixing of fluids containing biomolecules, such as proteins and DNAs, is calculated based on the maximum strain rate. It is seen that cylinder radius and flow behavior index strongly affect the shear-induced binary aggregation kinetics and the associated probability density distribution of particles, while the yield stress has a negligible impact on the same.

DOI: [10.1103/PhysRevFluids.9.023301](https://doi.org/10.1103/PhysRevFluids.9.023301)

I. INTRODUCTION

Microfluidics and microscale transport processes have received significant attention from the interdisciplinary research community due to their great many applications in chemical, biochemical, and biological processes [1–11]. Examples include drug delivery [12,13], DNA hybridization [14,15], sample separation [16,17], micromixing [18,19], biochemical analysis [20,21], etc. Typically, the candidate fluid(s) used in the arena of these applications is/are different biofluids [22–27]. The presence of plasma, red blood cells, white blood cells, protein molecules, DNAs, etc., alters the rheology of biofluids to exhibit non-Newtonian models in nature, while different non-Newtonian models are used to describe the rheological behavior of these fluids as well [22–27]. Apostolidis and Beris [26] explored that biofluid like blood consists of a significant value of yield stress, which leads to the alteration of its rheology exhibiting viscoplastic nature. Viscoplastic fluids can only flow if the stress exceeds a specific threshold, known as the yield stress. They reviewed that the yield stress

*Corresponding author: pranabm@iitg.ac.in; mail2pranab@gmail.com

is a function of the hematocrit level and fibrinogen concentration, while its value increases with the increase in both fibrinogen concentration and hematocrit level. It may be mentioned here that several researchers have employed the Herschel-Bulkley viscoplastic model to represent the rheology of biofluids mentioned above, and analyzed the effect of external forcing, viz., electrical force, rotational forces, on the underlying transport under the modulation physicochemical properties of the surface [28–33].

The micromixing phenomenon that concerns the mixing of exceedingly small volumes is an important functionality of different state-of-the-art microfluidic systems and devices used in the aforementioned applications [34,35]. This fluidic functionality at the microfluidic scale is largely governed by the interplay between molecular diffusion of the candidate fluids and the convective strength of the flow. For the typical range of molecular size (d) of proteins and DNAs [36,37], and the order of reference viscosity of 10^{-2} Pa s for shear-thinning fluids (μ_r^*) and using the Stokes-Einstein equation ($D = k_B T / 6\pi \mu_r^* d$), where T represents the reference temperature and k_B is the Boltzmann constant [38], the bound of the diffusion coefficient falls within the range of 10^{-12} – 10^{-10} m²/s [39,40]. When considering typical microfluidic length scales of $O(10\text{--}100)$ μm and electroosmotic flow velocities of $O(10^{-5})$ m/s, the diffusive Peclet number (Pe) for an electroosmotic flow configuration significantly exceeds unity ($\text{Pe} \gg 1$) for lower values of diffusive Peclet numbers. It is important to note that the diffusive Peclet number is commonly defined as the ratio of the diffusive timescale to the convective timescale, determined by characteristic length and velocity scales. Alternatively, it denotes the relative significance of convection compared to diffusion in terms of species transfer. This scale analysis is suggestive that the underlying mixing at small scale is expected to be dominated by convective strength even in the highly laminar regime of the electroosmotic flow (Reynolds number $\ll 1$) [40–42]. Accounting for this transport feature, the generation of vortices in the flow pathway of microfluidic devices and systems seems to be an avenue to increase the mixing efficiency. To this end, several studies have been conducted to examine the characteristics of vortices generated under the influence of surface charge heterogeneity or nonuniform zeta potential when an external electric field is applied across the fluidic pathway [40–43]. Here, it is important to note the zeta potential, also referred to as the potential at the shear plane. The potential is obtained at the interface between the stern layer and the diffused layer of ionic components within the electric-double layer generated by the interaction of an aqueous electrolyte solution and a charge surface. To modify the electrical forces in electroosmotically driven flows within a microchannel, one can manipulate the ionic distribution through variations in the nonuniform zeta potential [40–43]. In the paradigm of field driven forcing modulated mixing phenomena of both Newtonian and non-Newtonian (elastic, inelastic, and plastic) fluids, several authors have investigated the impact of fluid rheological and electrokinetic parameters on the underlying mixing strength, while aptly discussing mixing enhancement strategy as well [43–51].

A review of the state-of-the-art literature witnesses that the simple microfluidic channel with a built-in two-part cylinder having dissimilar zeta potential is able to generate vortex in the flow pathway under the influence of an external field [51,52]. It should be noted that the flow has a very low Reynolds number ($\ll 1$) since these vortices are generated in microfluidic channels. Consequently, these vortices are also referred to as laminar flow vortices [51,52]. Quite evidently, this vortex can be utilized for the enhancement of mixing at small-scale systems as well [51]. The impact of the intervening viscoplastic behavior, which is often exhibited by biofluids [22–27], and its interaction with the interfacial electrochemical phenomenon on the generation of vortices in a microfluidic channel has not yet been examined, despite having enormous significance of this kind of simple flow configuration toward ensuring augmented solute mixing through the formation of vortices therein. In this context, it is worth noting that a variety of interfacial electrochemical phenomena occur when electrolytic solutions come into contact with charged microfluidic walls. These phenomena encompass ion-electron transfer, molecular-ion adsorption and desorption, and complex interface remodeling [51,52]. In order to effectively mix viscoplastic fluids, the current work aims to investigate the interactive effect between the fluid rheology and laminar flow vortices

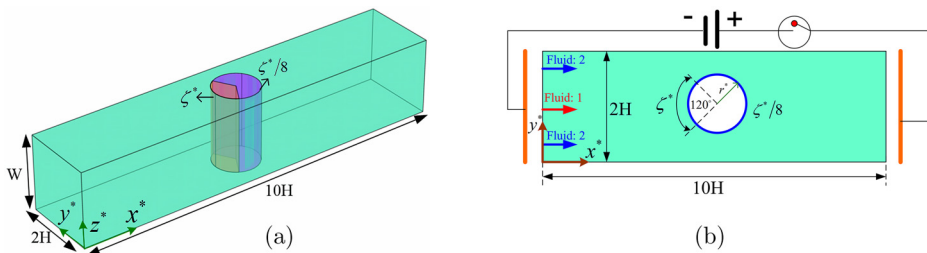


FIG. 1. (a) Three-dimensional view of the physical domain. (b) Cross-sectional view of the physical domain in the x^*y^* plane.

in a simple microchannel with a built-in two-part cylinder having different zeta potential at its upstream and downstream sides.

Furthermore, in the paradigm of non-Newtonian solute mixing, the shear-induced aggregation kinetics [40,53] has recently been extensively studied by several researchers [54–57]. Shear-induced irreversible aggregation is a common occurrence in the context of biological colloidal particles, such as cells, protein solutions, blood plasma, and macromolecules. Researchers have utilized the two-body Smoluchowski equation as a theoretical tool to investigate this intricate aggregation phenomenon. It has been found that the active cluster size produced by the aggregation kinetics triggers shear-driven aggregation. As a result, an explosive increase in viscosity under specific shear rates is predicted to occur after a critical period of time. This critical time is estimated based on the kinetic equation for the rate of change in particles, and it is determined by the reciprocal of the kinetic constant for the aggregation of the primary particles [53]. The thickness of the charged polyelectrolyte layer (PEL) is found to have a critical influence on the characteristic time for binary aggregation within the context of electroosmotic vortex production in micromixers. For alternate PEL arrangements at the top and bottom walls with a thinner PEL, the characteristic time for binary aggregation is greater. However, when the PEL is arranged side by side on the walls and is thicker, the characteristic time for binary aggregation is higher [40]. Recent research has highlighted the significance of non-Newtonian shear-thinning liquid rheological parameters on the characteristic time for binary aggregation, which is attributed to electroosmotic vortex generation by zeta potential patterning in micromixers with cylinders [51]. This aspect is found to be of practical significance in characterizing mixing when dealing with non-Newtonian fluids and solutes containing colloidal particles. Following this direction, the present work also critically discusses how the viscoplastic nature affects aggregation kinetics.

II. THEORETICAL MODEL

The schematic diagram of the present micromixer is depicted in Fig. 1. The height, length, and width of the micromixer are taken as $2H$, $10H$, and W , respectively. Here, the width of the micromixer is significantly larger than its height ($W \gg 2H$). Therefore, as depicted in Fig. 1(a), a two-dimensional flow model [50] is employed in this analysis. It may be mentioned here that three-dimensional real-world systems can be modeled by a cost-effective two-dimensional model under certain conditions without gross Comptonization. For a nearly constant effect (almost invariant) of the underlying physical phenomenon along any specific axis, it is reasonable to presume that the physics being analyzed on that axis can be accurately reproduced by the justified approximations of prevalent physical phenomena therein. Consequently, under these circumstances as considered in seminal works [33,40,51,52], a two-dimensional model can be assumed to mimic a three-dimensional physical phenomenon quite effectively. A two-part cylinder with radius r^* , having dissimilar values of surface potential with the same sign in its two parts, is placed inside the micromixer. In order to get a faster as well as an efficient mixing by the formation of

vortices adjacent to the cylinder (i.e., better mixing quality and desired flow rate), the magnitude of the zeta potential at the upstream side ($\zeta_U^* = \zeta^*$) is taken as eight times higher than that of the downstream side ($\zeta_D^* = \zeta^*/8$) [51,52]. According to Ref. [51], using $\zeta_D^* = \zeta^*/8$ allows for greater vortex strength, which can be advantageous in situations dominated by convection for mixing. Also, to obtain a larger size of the recirculation zone, the arc angles at the upstream and downstream sides are taken as 120° and 240° , respectively [51,52]. Moreover, the tracer fluid (fluid 1) is inserted at the intermediate part of the micromixer inlet, while the pure fluid (fluid 2), which has the same thermophysical properties as fluid 1, is inserted at the upper and lower parts of the inlet. For the chosen configuration of the micromixer, the flow is actuated by the application of an external electric field, leading to the potential difference ΔV across the micromixer ends. We have assumed that the flow is steady, incompressible, and two-dimensional. Also, the thermophysical properties are considered to be temperature independent as the temperature rises (<10 K) because Joule heating is ignorable for the order of external electric field intensity $\sim 10\,000$ V/m [58,59]. Moreover, the order of induced electric field [due to the electrical double-layer (EDL) phenomenon] is much higher than the externally applied electric field [51]. Therefore, the ionic distribution inside the EDL is independent from the external electric field. Additionally, in the current context, the ionic Peclet number ($Pe_i = HU_{HS}^*/D_i < 1$) is very small due to the velocity scale, characteristic length scale (H), and order of ionic diffusion coefficient (D_i). Here, U_{HS}^* is the reference Helmholtz-Smoluchowski velocity. Hence, the ionic distribution is independent from the convective field as well. Considering the physically justified assumptions as discussed above, the following dimensionless equations are used to compute the external potential, EDL potential, flow, and species concentration fields, respectively:

Laplace equation:

$$\nabla^2 \phi = 0, \quad (1)$$

where ϕ is the dimensionless external potential normalized by the scale $\Delta VH/L$ [42,43,51].

Poisson-Boltzmann equation:

$$\nabla^2 \psi = \kappa^2 \sinh(\psi). \quad (2)$$

The EDL potential field is represented by ψ in the present case and is normalized by scale $k_B T/ze$.

Continuity equation:

$$\nabla \cdot \mathbf{U} = 0. \quad (3)$$

Momentum equation:

$$\text{Re}(\mathbf{U} \cdot \nabla)\mathbf{U} = -\nabla P + \nabla \cdot \boldsymbol{\tau} + \frac{\kappa^{n+1}}{n^n} \sinh(\psi) \nabla(\phi + \psi/\Lambda). \quad (4)$$

Here, the dimensionless velocity vector, local pressure, and deviatoric stress tensor, respectively, are represented in the aforementioned equation by \mathbf{U} , P , and $\boldsymbol{\tau}$.

Species transport equation:

$$\nabla^2 C = \text{Pe}(\mathbf{U} \cdot \nabla C). \quad (5)$$

Here, C stands for species concentration in its dimensionless form. It is important to note that the scaling reference species concentration (C_{ref}^*) used here corresponds to the species concentration in fluid 1 ($C_{\text{ref}}^* = C_1^*$) at the inlet. In all cases, a constant species concentration in fluid 1 is considered.

Moreover, the dimensionless external potential, dimensionless EDL potential, dimensionless velocity vector, dimensionless pressure, and dimensionless species concentration, respectively, are expressed in terms of its dimensional form as

$$\begin{aligned} \phi &= \phi^* L / \Delta VH, & \psi &= \psi^* ze / k_B T, & \mathbf{U} &= \mathbf{U}^* / U_{HS}^* = u \hat{i} + v \hat{j}, \\ P &= P^* H / \mu_r^* U_{HS}^*, & \text{and } C &= C^* / C_{\text{ref}}^*. \end{aligned} \quad (6a)$$

In Eqs. (1)–(5), the del operator, ∇ , is written as

$$\nabla \equiv (\hat{i}\partial/\partial x + \hat{j}\partial/\partial y) \equiv H(\hat{i}\partial/\partial x^* + \hat{j}\partial/\partial y^*). \quad (6b)$$

Here, note that the superscript “*” represents the dimensional quantity.

The dimensionless Debye parameter (κ), Debye length (λ_D) and bulk ionic number concentration (n_o) are expressed as

$$\kappa = H/\lambda_D, \quad \lambda_D = \sqrt{\varepsilon_r \varepsilon_o k_B T / z^2 e^2 n_o}, \quad n_o = 1000 N_A M_c. \quad (6c)$$

Here, λ_D , M_c , and N_A are Debye length, molarity of the ionic solution of monovalent ions, and Avogadro’s number, respectively. Also, ε_r , ε_o , k_B , T , $z(=z^+ = z^-) = 1$, and e are relative permittivity of the fluid, electric permittivity of the free space, Boltzmann constant, reference absolute temperature, valency of the ions, and charge of a single electron, respectively.

The reference Helmholtz-Smoluchowski velocity (U_{HS}^*) for normalizing the velocity field can be written as [30,33]

$$U_{HS}^* = n(\lambda_D)^{(n-1)/n} (\varepsilon_o \varepsilon_r E_{\text{ref}} \psi_{\text{ref}}^* / m)^{1/n}. \quad (6d)$$

Here, the reference zeta potential and reference electric field are expressed as

$$\psi_{\text{ref}}^* (= k_B T / z e), \quad E_{\text{ref}} (= \Delta V / L). \quad (6e)$$

Also note that n and m are the flow behavior index and flow consistency index, respectively.

The dimensionless deviatoric stress tensor scaled by $m(U_{HS}^*/H)^n$ and expressed as

$$\boldsymbol{\tau} = \eta(\dot{\gamma})((\nabla \mathbf{U}) + (\nabla \mathbf{U})^T), \quad (7)$$

$$\dot{\gamma} = 1/2 \mathbf{S} : \mathbf{S}. \quad (8)$$

Here, $\dot{\gamma}$ is the dimensionless second invariant of the rate of deformation tensor and the strain rate tensor is represented as

$$\mathbf{S} (= [(\nabla \mathbf{U}) + (\nabla \mathbf{U})^T]) \quad (9)$$

The ratio of reference external and reference EDL potential is represented as [51]

$$\Lambda (= E_{\text{ref}} H / \psi_{\text{ref}}^*). \quad (10)$$

Moreover, following the Herschel-Bulkley model with Papanastasiou modification [60,61], the apparent viscosity [$\eta^*(\dot{\gamma}^*)$] can be written as

$$\eta^*(\dot{\gamma}^*) = \frac{\tau_y^*}{\dot{\gamma}^*} [1 - \exp(-M_p^* \dot{\gamma}^*)] + m(\dot{\gamma}^*)^{n-1} \quad \text{for } \tau^* > \tau_y^*, \quad (11a)$$

$$\dot{\gamma}^* = 0 \quad \text{for } \tau^* < \tau_y^*. \quad (11b)$$

Here, M_p^* and τ_y^* are stress growth parameters proposed by Papanastasiou and Boudouvis [60,61] and yield stress, respectively. Now, using the reference viscosity scale $\mu_r^* = m(U_{HS}^*/H)^{n-1}$, the dimensionless apparent viscosity can be written as

$$\eta(\dot{\gamma}) = \frac{\text{Bn}}{\dot{\gamma}} [1 - \exp(-M_p \dot{\gamma})] + (\dot{\gamma})^{n-1} \quad \text{for } \tau > \text{Bn}, \quad (12a)$$

$$\dot{\gamma} = 0 \quad \text{for } \tau < \text{Bn}. \quad (12b)$$

It is worth noting that the curve-fitting parameters for the plot of apparent viscosity and shear rate, often derived from experiments, are the flow behavior index (n) and the flow consistency index (m). Furthermore, by extrapolating the fitted polynomial at zero shear rate, the yield stress value can be determined if a polynomial equation is fitted to the nonlinear stress-strain experimental data. The growth rate parameter can also be found using the best fitted experimental stress-strain curve. In

Eqs. (12a) and (12b), the dimensionless stress growth parameter (M_P) and Bingham number (Bn), respectively, are expressed as

$$M_P = M_P^* U_{HS}^* / H \quad \text{and} \quad \text{Bn} = \tau_y^* / m (U_{HS}^* / H)^n \quad (12c)$$

Also, the Reynolds number and diffusive Peclet number, respectively, appearing in Eqs. (4) and (5) are expressed as

$$\text{Re} = \rho U_{HS}^* H / \mu_r^* \quad \text{and} \quad \text{Pe} = U_{HS}^* H / D. \quad (12d)$$

We have used the following boundary conditions to solve the aforementioned dimensionless governing transport equations.

At the inlet:

$$\begin{aligned} \mathbf{n} \cdot \nabla \psi = 0, \quad \phi = 0, \quad P = P_{\text{atm}}, \quad C = 1 \quad \text{for } 0.6 \leq y \leq 1.4, \quad \text{and} \\ C = 0 \quad \text{for } y < 0.6 \quad \text{and} \quad y > 1.4. \end{aligned} \quad (13a)$$

In this instance, it is important to note that the boundary condition $C = 1$ for $0.6 \leq y \leq 1.4$ was selected to achieve a uniformly mixed state (C_∞) with a final composition of 50% of fluid 1 and 50% of fluid 2, i.e., C_∞ approaches 0.5 in the final mixed state.

At the outlet:

$$\mathbf{n} \cdot \nabla \psi = 0, \quad \phi = 10, \quad P = P_{\text{atm}}, \quad \text{and} \quad dC/dx = 0. \quad (13b)$$

At the plane wall:

$$\mathbf{n} \cdot \nabla \psi = 0, \quad \mathbf{n} \cdot \nabla \phi = 0, \quad \mathbf{U} = 0, \quad \text{and} \quad dC/dy = 0. \quad (13c)$$

At the cylinder wall:

$$\psi_U = \zeta_U^* z e / k_B T, \quad \psi_D = \zeta_D^* z e / k_B T, \quad \mathbf{n} \cdot \nabla \phi = 0, \quad \mathbf{U} = 0, \quad \text{and} \quad dC/d\chi = 0. \quad (13d)$$

Here, \mathbf{n} is the normal unit vector to the surface and χ is the normal direction to the cylinder wall.

The net throughput associated with the bulk flow in its dimensionless (Q) form can be expressed as [51]

$$Q = \int_{y=0}^{y=2} u \, dy. \quad (14)$$

Here, $Q = Q^* / Q_{\text{ref}}^*$; Q^* is the flow rate per unit width and $Q_{\text{ref}}^* (= U_{HS}^* H)$ is the reference scale for flow rate per unit width.

Further, the mixing quality at the outlet of the mixer is quantified in terms of mixing efficiency (η) and given as [50,51]

$$\eta = \left[1 - \left(\int_{y=0}^{y=2} |C - C_\infty| \, dy \right) / \left(\int_{y=0}^{y=2} |C_o - C_\infty| \, dy \right) \right] \times 100\%, \quad (15)$$

where $C_o (= 0$ or $1)$ and C_∞ represents the purely unmixed ($\eta = 0\%$) and mixed state ($\eta = 100\%$), respectively. It should be noted in this context that the value of C_∞ relies on the inflow rate of the tracer liquid. By changing the rheological and geometrical parameters, it is anticipated that the electroosmotic flow velocity profile at the inlet will be distinct. In light of the local velocity field at the entrance, we have defined the expression of C_∞ as follows:

$$C_\infty = \frac{\int_{y=0}^{y=2} u C \, dy}{\int_{y=0}^{y=2} u \, dy}. \quad (16)$$

TABLE I. Mixing efficiency at the different mesh system (M) for $\zeta = 4$, $r = 0.7$, $\text{Bn} = 0.25$, $\kappa = 30$, $\text{Pe} = 250$, and $n = 0.5$.

Mesh system (M)	Number of elements	Mixing efficiency	Error (%)
$M1$	5789	77.14	2.71
$M2$	9968	77.45	3.12
$M3$	25204	75.845	0.99
$M4$	62266	75.096	0.01
$M5$	109038	75.104	0

III. NUMERICAL METHODOLOGY AND MODEL VALIDATION

The dimensionless governing transport equations [Eqs. (1)–(5)] are numerically solved using the finite element method-based solver COMSOL MULTIPHYSICS. Consistent with this solver, the nonuniform triangular mesh elements divide the physical domain into subdomains. In Appendix A, we have provided an illustration of the mesh structure. To accurately predict the sharp EDL potential gradient, ψ , and velocity gradient, we employ a denser mesh closer to the cylinder wall. Additionally, the mesh is denser in regions with discontinuities in the zeta potential boundary condition (see zoomed view of the mesh structure in the bottom-right section of Appendix A) and near the species concentration boundary condition at the inlet (see zoomed view of the mesh structure in the bottom-left section of Appendix A). The dimensionless element size near the cylinder wall and plane wall falls within the range of 0.005 to 4×10^{-5} , except in the region of zeta potential and species concentration boundary condition discontinuity, where the range is 0.001 to 4×10^{-5} . It is worth noting that the distinctive dimensionless EDL thickness is predominantly found in the normal region with a dimensionless length of $1/\kappa$, which is calculated as 0.033 33 for $\kappa = 30$. The mesh element sizes considered for the EDL region (ranging from 0.005 to 4×10^{-5}) are much smaller than 0.033 33. As a result, we can confidently assert the accuracy of the expected EDL potential gradient. Additionally, we apply the Galerkin weighted method [62–64] to convert the governing differential equations into integral equations, which are then iteratively solved until we reach the relative residual condition of 10^{-6} for all transport variables. Further, the grid independence test is performed by calculating mixing efficiency at the mixer outlet for higher cylinder radius ($r^*/H = r = 0.7$), while other parameters considered are $n = 0.5$, $\text{Bn} = 0.25$, $\kappa = 30$, and $\text{Pe} = 250$. The grid test results are presented in Table I. A closer look at Table I discloses that the results insignificantly change (by less than 1%) as the number of elements increases from 62 266 to 109 038, while other variables remain the same. Therefore, for the current numerical analysis, we consider 62 266 mesh elements.

We have compared the efficacy of the numerical model employed here by comparing the present results with both the existing experimental and theoretical results from different perspectives. First, as presented in Fig. 2(a), the flow velocity profile obtained from our analysis for Newtonian fluid ($n = 1$, $\text{Bn} = 0$) and Bingham plastic fluid ($n = 1$, $\text{Bn} = 0.5$, $M_P = 500$), under the electroosmotic actuation through the parallel plate microchannel, is compared with the result of Qi and Ng [32] when $\kappa = 10$. This validation verifies the accuracy of the electroosmotic flow field's yield stress impact. Next, in Fig. 2(b), the average electroosmotic flow (EOF) velocity for the flow of non-Newtonian fluid through a plane microchannel obtained at the different electric field intensity is compared with the experimental result of Huang *et al.* [65] for the zeta potential -24 mV in the limiting case $\text{Bn} = 0$. These findings were generated by Huang *et al.* [65] in the context of electroosmotic flow within a rectangular planar microchannel using an aqueous NaCl-polyethylene oxide solution. This benchmarking process validates the prediction made by the current numerical model regarding the impact of shear-thinning behavior on electroosmotic flow. Further, as shown in Fig. 2(c), the normalized species concentration at the outlet of the plane electroosmotic micromixer is validated with the result of Biddiss *et al.* [39] for the electric field strengths 70 and 280 V/cm

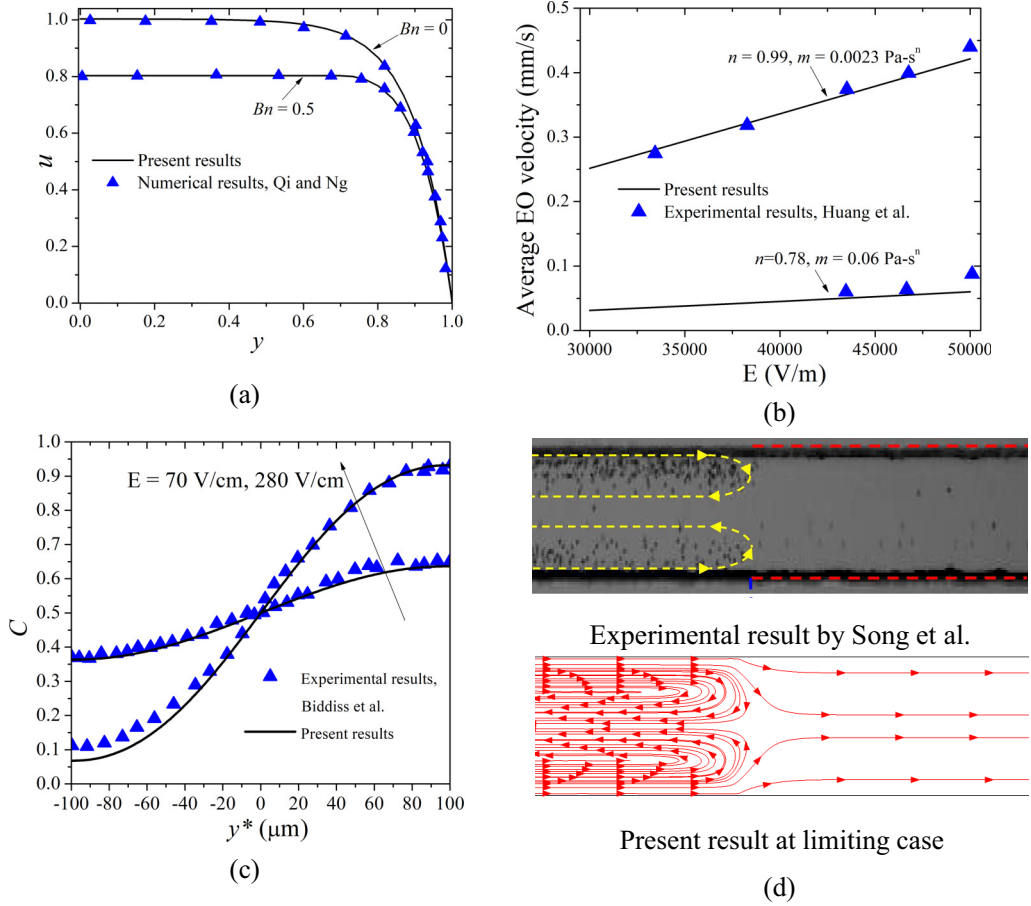


FIG. 2. (a) Comparison of flow velocity profile for Newtonian fluid ($n = 1, Bn = 0$) and Bingham plastic fluid ($n = 1, Bn = 0.5, M_p = 500$) with the result of Qi and Ng [32] for $\kappa = 10$. (b) Comparison of experimental average electroosmotic flow (EO) velocity for the flow of non-Newtonian fluid through a plane microchannel at the different electric field intensity (E) with the experimental result of Huang *et al.* [65] for the zeta potential -24 mV at the limiting case $Bn = 0$. (c) Comparison of normalized species concentration at the outlet of the plane electroosmotic micromixer with the result of Biddiss *et al.* [39] for the electric field strengths 70 and 280 V/cm at the limiting case $n = 1, Bn = 0$. (d) Comparison of flow field in the PDMS microchannel having a modified section zeta potential of -5 mV (left) and an untreated PDMS side zeta potential of -60 mV (right side) with the experimental result by Song *et al.* [66] at limiting case $n = 1$ and $Bn = 0$.

in the limiting cases $n = 1$ and $Bn = 0$. Finally, we have attempted to benchmark the formation of electroosmotic vortices by leveraging the discontinuity in zeta potential difference at the wall. Hence in Fig. 2(d), we have compared the flow field in a Polydimethylsiloxane (PDMS) plane microchannel having a modified section zeta potential of -5 mV (left side of the channel) and an untreated PDMS side zeta potential of -60 mV (right side of the channel) with the experimental results of Song *et al.* [66]. For this benchmarking, the microchannel is set to have a width and length of 70 and 2000 μm , respectively. The ratio of the length of the modified section to the untreated section is chosen as 4, with the liquid density and viscosity set at 1000 kg/m^3 and $0.001 \text{ Pa}\cdot\text{s}$, respectively. For this part, we have considered a limiting case of $n = 1$ and $Bn = 0$ to obtain the numerical results. The benchmarking results presented in Figs. 2(a)–2(d) underline the accuracy

of the current numerical framework, which makes it suitable for further calculation as discussed systematically in the forthcoming sections.

IV. RESULTS AND DISCUSSION

A. Range of parameters

For the present study, we have taken micromixer half height as $H = 50 \mu\text{m}$. We consider fluids commonly used in microfluidic devices, such as blood, DNAs solutions, or polymeric solutions, which exhibit shear-thinning behavior ($n < 1$) and have decreasing apparent viscosities at higher shear rates [67–69]. In this context, a range of flow behavior index ($0.5 \leq n \leq 1$) values is considered, and similar ranges are employed in Refs. [28–33]. Here, it should be emphasized that when $n = 1$, it denotes that the solution exhibits Newtonian behavior. The flow consistency index for biofluids such as blood and density of the aqueous solution are taken as $m = 0.017 \text{ Pa} \cdot \text{s}^n$ [27] and $\rho = 1000 \text{ kg m}^{-3}$ [51], respectively. The values of the reference electric field (E_{ref}), reference EDL potential (ψ_{ref}^*), upstream side zeta potential (ζ_U^*), and relative electric permittivity of the fluid medium (ε_r) are taken as 10000 V m^{-1} , -25 mV , -100 mV , and 80 , respectively [51]. Consequently, the reference Helmholtz-Smoluchowski velocity, $U_{HS}^* (= n(\lambda_D)^{(n-1)/n} (\varepsilon_0 \varepsilon_r E_{\text{ref}} \psi_{\text{ref}}^* m)^{1/n})$, is obtained from 1.04118×10^{-5} to $3.25214 \times 10^{-5} \text{ m/s}$. For the aforementioned range of flow behavior index and for the typical Debye parameter value for the microfluidic channels, $\kappa (= H/\lambda_D) = 30$ [28,41,43]. As a result, we can say that the reference velocity order is $\sim 10^{-5} \text{ m/s}$. Pertaining to microfluidic applications, the order of yield stress (τ_y^*) for the non-Newtonian fluid is obtained as 1 mPa [22,26]. Hence, given the range of dependent geometrical and fluidic parameters taken into consideration, the value of the Bingham number [$\text{Bn} = \tau_y^*/m(U_{HS}^*/H)^n$] approaches close to 0.25 . Accordingly, the range $0 \leq \text{Bn} \leq 0.25$ as considered here, is appropriate for numerical simulations. Additionally, it is worth noting that Biddiss *et al.* [39] expected species diffusion coefficients in the range of $10^{-10} \text{ m}^2/\text{s}$, while Gaikwad *et al.* [40] mentioned values up to $10^{-12} \text{ m}^2/\text{s}$. Hence, the order of the species diffusive Peclet number ($\text{Pe} = U_{HS}^* H/D$) is determined to be in the range of 1 – 1000 , considering the examined range of U_{HS}^* and the order of H , as well as the order of species diffusion coefficient ranging from $10^{-12} \text{ m}^2/\text{s}$ to $10^{-10} \text{ m}^2/\text{s}$. These previous studies pertinent to microfluidics [42,51] have also investigated a similar spectrum of diffusive Peclet numbers. Moreover, the dimensionless cylinder radius ($r = r^*/H$) is varied in the range of $0.3 \leq r \leq 0.7$. The value of M_P should be higher to yield convergence and should not be so high that it reduces the convergence speed [29,30,32,33]. Therefore, the effect of M_P on the underlying transport is presented in Appendix B. As found from the tabulated data in Appendix B, the effect of M_P on flow rate and recirculation velocity is miniscule. Consequently, we have taken a constant $M_P (=500)$ for the numerical simulations of this analysis.

B. Flow field

When $\text{Bn} = 0$ and 0.25 , Fig. 3(a) shows the streamlines and contours of dimensionless flow velocity close to the cylinder. The stream function is computed by solving the equation $\nabla^2 \Psi = -(\partial v/\partial x - \partial u/\partial y)$ and by using the developed flow field, while $\Psi = 0$ is imposed at the bottom wall. Note that consideration leading to $\Psi = 0$ follows from the fact that the flow rate between two streamlines tends to zero near the wall due to the no-slip condition. It is observed from Fig. 3 that vortices are formed in the region closer to the wall at the upstream end of the cylinder. Here, it should be mentioned that a stronger EOF field is generated at the upstream cylinder wall, attributed primarily to the higher electroosmotic actuation caused by the larger magnitude of zeta potential therein (see Fig. 1). On the other hand, due to the absence of EDL, there is no driving force for the liquid mass close to the plane wall. Hence, due to a substantial viscous resistance between the plane and upstream cylinder walls caused by the sharper velocity gradient, vortices are formed as witnessed in Fig. 3(a). Further, the effect of Bn on the flow velocity profile near the inlet

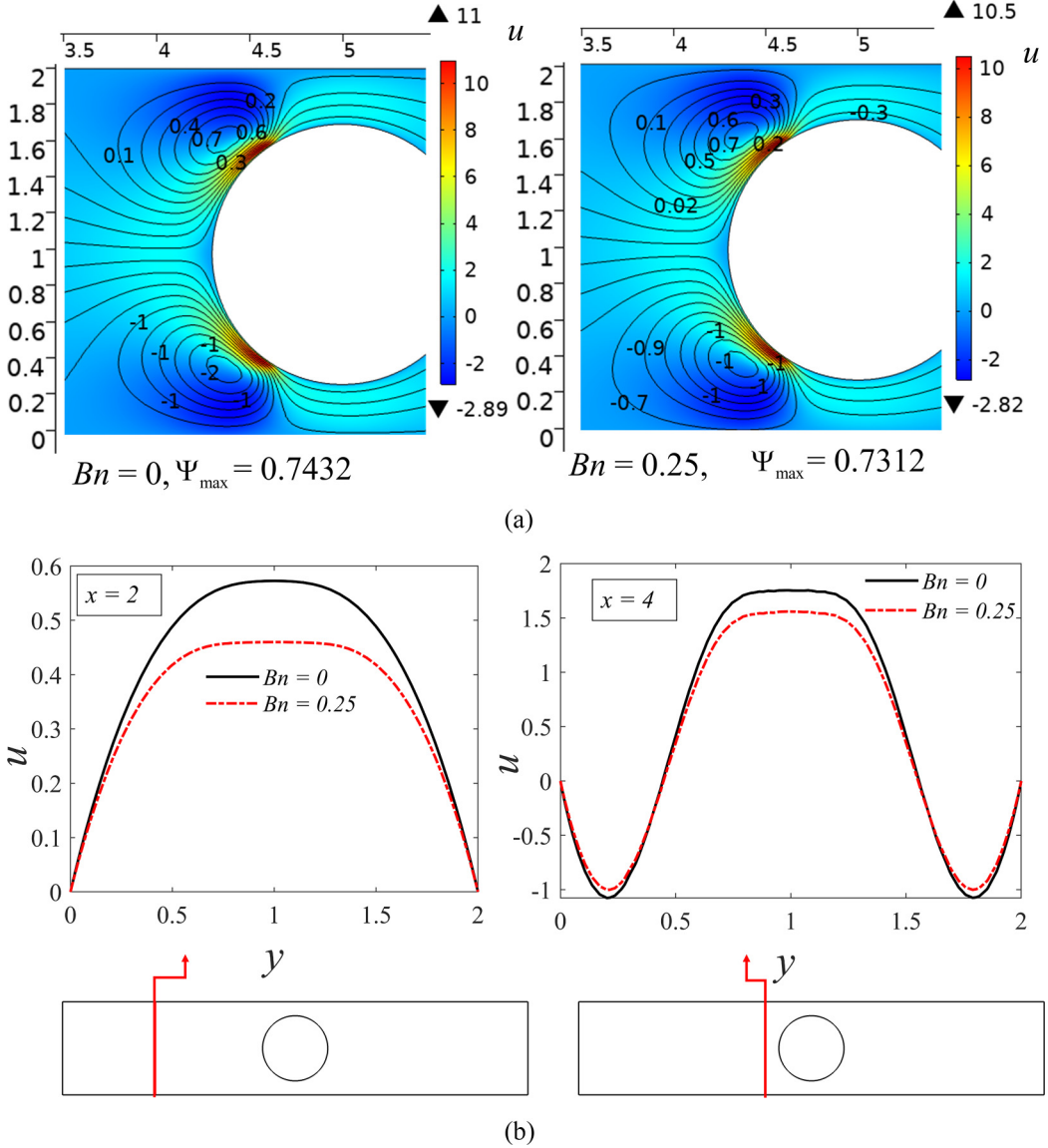


FIG. 3. (a) Contours of streamlines and dimensionless flow velocity for (a) $Bn = 0$ and $Bn = 0.25$ when $r = 0.7$ and $n = 0.5$. (b) Dimensionless flow velocity profile at sections $x = 2$ and 4 at different Bn when $r = 0.7$ and $n = 0.5$.

and cylinder is depicted in Fig. 3(b) at sections $x = 2$ and 4 , respectively. We can observe that the inherent yield stress for $Bn = 0.25$ reduces the core flow velocity as compared to $Bn = 0$ at $x = 2$. Also, the core flow velocity profile is flatter at $Bn = 0.25$, attributed to the presence of an unyielded region in the core. This observation shows similarity with the established work as well [33]. Moreover, due to the reduction in core region flow velocity, and consequently, the reduction in velocity gradient between the fluid elements near the cylinder and plane walls, the viscous resistance decreases as well. Notably, this reduction in viscous resistance for $Bn = 0.25$ causes a mild decrease of viscous resistance-induced recirculation strength (Ψ_{\max}) [see Fig. 3(a)] and magnitude of reversed

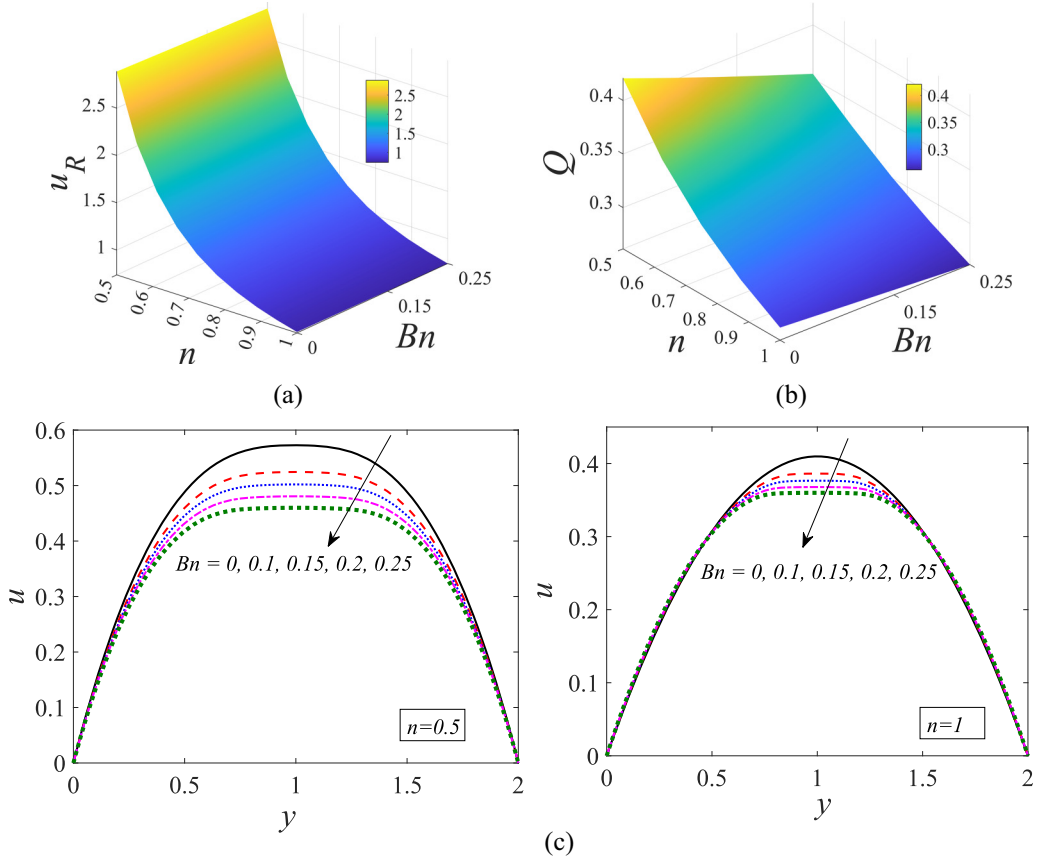


FIG. 4. Variation of (a) dimensionless recirculation velocity (u_R) and (b) dimensionless flow rate (Q) in the plane of n and Bn when $r = 0.7$. (c) Dimensionless flow velocity profile at $x = 2$ at different Bn when $n = 0.5$ (left) and 1 (right).

flow velocity [see Fig. 3(a)]. These two observations, as depicted in Fig. 3(a), are witnessed when comparing with the similar variation for $Bn = 0$.

The variation of recirculation velocity (u_R) in the plane of Bn and n is shown in Fig. 4(a). It is noted that u_R represents the magnitude of maximum reversed flow velocity in the domain as defined in previous works [51,52]. We observe that as n increases, the value of u_R decreases. The apparent viscosity increases with n for shear-thinning viscoplastic fluids, which in turn, results in a reduction in flow velocity. Therefore, the velocity gradient of the fluid elements between near-plane wall and cylinder, accounting for this reduction in flow velocity, decreases with n as well. Consequently, with increasing n , the intensity of the viscous resistance-induced recirculation velocity decreases. Additionally, as witnessed in Fig. 3, an insignificant change in recirculation strength with a change in Bn from 0 to 0.25 (see Fig. 3) underlines almost no effect of Bn on u_R .

In the paradigm of low Re ($\ll 1$) transport, solute mixing can be either convection or diffusion dominated based on the scale of diffusive Peclet number dependent on the species diffusion coefficient. For smaller values of the species diffusive Peclet number (< 1), molecular diffusion predominates in mixing. In contrast, mixing is essentially convection dominated at larger values of the diffusive Peclet number ($\gg 1$), which is heavily controlled by the underlying flow velocity. A relatively higher flow velocity, although it will result in a higher flow rate, may have an adverse impact on the mixing efficiency in the regime of low Re transport. Thus, pertaining to microscale

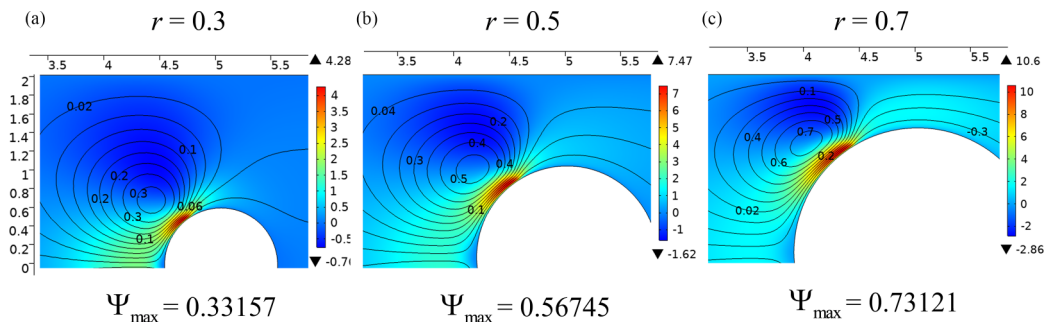


FIG. 5. Contours of streamline and dimensionless flow velocity contour for (a) $r = 0.3$, (b) $r = 0.5$, and (c) $r = 0.7$ when $Bn = 0.25$ and $n = 0.5$. The legend of dimensionless flow velocity (u) is shown in the right side of the image.

transport, obtaining a desirable solute mixing implicates a compromised flow rate as well. To illustrate how changes in the dimensionless flow rate (Q) may affect the solute mixing process, which will be discussed in the coming sections, we have depicted this variation in Fig. 4(b) in the plane of n and Bn . We can observe that the magnitude of Q decreases with increasing the value of n . It is because of the increase in apparent viscosity with n , that the intensity of the primary flow velocity decreases. Thus, it is intuitive to find a decrease in Q with n in Fig. 4(b). Additionally, a decrease in Q with Bn is due to the reduction in core region flow velocity (see Fig. 3). It is indeed interesting to note that when n decreases, Q decreases with Bn at a higher rate. The explanation behind this observation is as follows. As demonstrated in Fig. 4(c), lower n ($=0.5$) provides a sharper velocity gradient toward the plane wall as compared to the higher n ($=1$). This observation is attributed to the smaller apparent viscosity near the plane wall for lower n . As a result, the flatter core flow velocity field is obtained for smaller n . As seen in Fig. 4(c), the decrease in core region velocity with Bn is therefore anticipated up to a longer transverse length for a lower n . What follows from this observation is that for the viscoplastic fluid having shear-thinning nature, the flow rate drops with Bn and the rate of decrement is higher when the shear-thinning nature is higher (i.e., smaller n).

In Fig. 5, which depicts the contours of a dimensionless flow field and streamlines, the effect of the dimensionless cylinder radius (r) on the flow field is shown. It has been found that when r increases, the intensity of the maxima flow velocity increases. The electroosmotic body force and, consequently, the velocity magnitude are enhanced by an increase in the electric field intensity with r (see Appendix C). Additionally, when r increases, the recirculation zone's strength increases. The increase in viscous resistance with r between the plane wall and cylinder is attributed to this observation. In particular, this phenomenon facilitates flow reversal with greater strength at a larger radius.

C. Yielded–unyielded region

Figure 6 shows the contours of the yielded and unyielded regions and streamlines at various cylinder radii (r). The yielded and unyielded regions are defined as being the region having above and below the critical dimensionless yield stress, $|\tau|_{\text{cri}} = Bn$, and adopted from Ref. [33]. Due to the flatter velocity profile (see Figs. 3 and 4), we notice that the unyielded zone is present close to the inlet and outlet side core section. Also, as r is increased, the thickness of the unyielded zone reduces, attributed primarily to the more concave velocity profile (see Appendix C) in the section at larger r . An increase in primary flow intensity, developed due to a stronger electric field at bigger r (see Appendix C), leads to the formation of a more concave velocity profile in the field as shown in Appendix C.

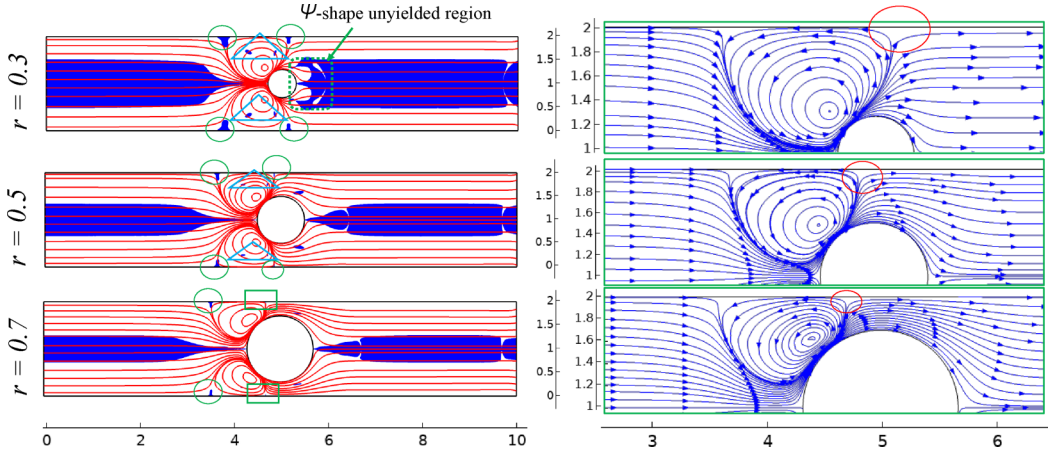


FIG. 6. Contours of yielded (white background) and unyielded (dark blue) regions with streamlines at different cylinder radius (left) and the corresponding zoomed view of streamline contours near the top part of the cylinder upstream and downstream (right) when $\zeta = 4$, $Bn = 0.25$, $\kappa = 30$, and $n = 0.5$.

Furthermore, the presence of a stagnation zone between the recirculation region and the primary flow close to walls (see the elliptical boxes in the contours of the streamline on the right side of Fig. 6) permits the creation of a smaller unyielding region (see the elliptical boxes in the contours of the yielded and unyielded regions on the left side of Fig. 6). Also, due to the larger strength of both primary and secondary flows at higher radius (see Fig. 5), the size of the unyielded region becomes relatively smaller due to the shrinkage in the stagnation region (see the elliptical boxes in the contours of the streamlines on the right side of Fig. 6). Notably, the unyielded zone disappeared on the downstream side of the vortex. This can be observed by examining the rectangular boxes corresponding to $r = 0.7$ in the contours of the yielded and unyielded regions on the left side of Fig. 6, and the same phenomenon applies to $r = 0.7$ for the same reason. Additionally, when the radius is smaller (at $r = 0.3$ and 0.5), we see smaller unyielded regions inside of the reversed flow field (see the triangular boxes in the contours of the yielded and unyielded regions on the left side of Fig. 6) where the shear stress is less than the yielding limit. In contrast, it is not observed for a larger radius ($r = 0.7$) because the greater shear rate results in a higher shear stress value (greater than the yielding limit). Additionally, a “ ψ ”-shaped unyielded region appeared in the downstream side of the cylinder when $r = 0.3$ (see the dotted rectangular box for $r = 0.3$ in the contours of the yielded and unyielded regions on the left side of Fig. 6). As seen from Fig. 6, for $r = 0.3$, the streamlines are aligned toward the plane wall near the top and bottom ends of the cylinder while they are directed toward the core in the downstream side of the cylinder (see the contour of the streamline on the right side of Fig. 6 for $r = 3$ in downstream). This type of arrangement of streamlines (flow structure) leads to a weaker shear stress between the regions. Also, the stagnant zone generated near the extreme downstream end of the cylinder causes the creation of an unyielded region therein, and hence a ψ -shaped unyielded region appeared in downstream at $r = 0.3$. Moreover, the region having weaker shear stress is smaller for higher radius ($r = 0.5$ and 0.7) due to the relatively stronger flow strength (see Fig. 5), which allows separate smaller unyielded regions to form near the top and bottom downstream regions of the cylinder.

D. Effect of yield stress on concentration field and mixing efficiency

Figures 7(a) and 7(b) plot the dimensionless species concentration contour for smaller ($Pe = 10$) and higher ($Pe = 500$) diffusive Peclet number, respectively. The variations depicted in Figs. 7(a) and 7(b) are obtained from different Bn and corresponding $n = 0.5$. It can be seen from Fig. 7(a)

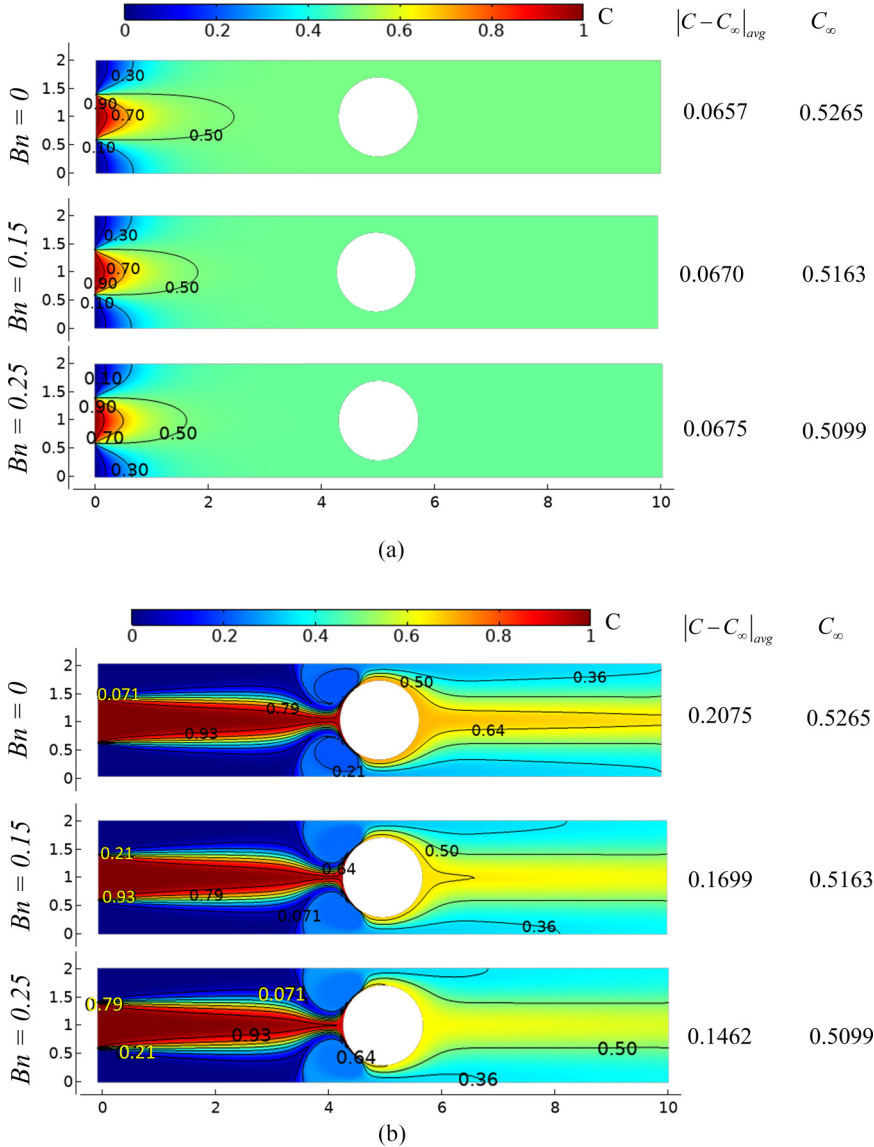


FIG. 7. Contours of dimensionless species concentration contours at different Bn when (a) $Pe = 10$ and (b) $Pe = 500$ when $r = 0.7$ and $n = 0.5$. The corresponding average deviation in concentration field over the fully mixed condition ($C = C_\infty$) i.e., $|C - C_\infty|_{avg}$ is presented in the right side of the image.

that with an increase in Bn , the tracer fluid concentration reaches up to a smaller distance in the downstream direction. This observation is attributed primarily to the reduction in core flow velocity with Bn [see Fig. 4(a)], which eventually reduces the strength of species concentration in the core region. On the other hand, as seen in Fig. 7(a), the value of C_∞ can decrease due to the reduction in inlet flow velocity associated with an increase in Bn [see Fig. 4(c)]. Conversely, as depicted on the right side of Fig. 7(a), the value of $|C - C_\infty|_{avg}$ is enhanced as C_∞ decreases with increasing Bn . It may be mentioned here that the systematic difference of $|C - C_\infty|_{avg}$ is due to the diffusive flux at the inlet. Accordingly, it can be concluded that the species concentration uniformity, relative to C_∞ , decreases with increasing Bn at $Pe = 10$. On the other hand, a higher Pe ($=500$) allows

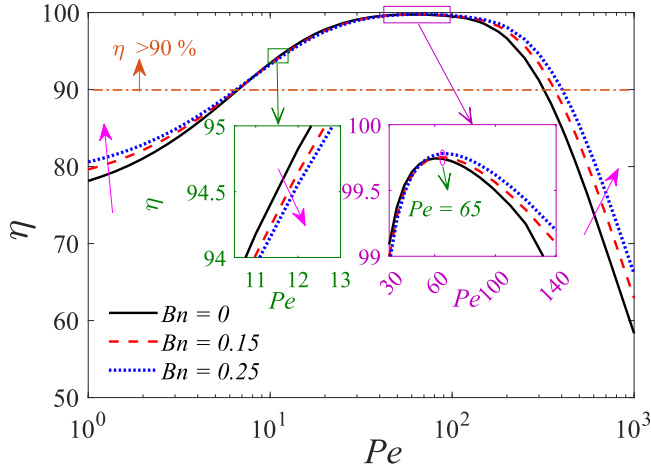


FIG. 8. Variation of mixing efficiency with Pe at different Bn when $r = 0.7$ and $n = 0.5$. The critical diffusive Peclet number corresponds to the maxima mixing efficiency and is obtained as $Pe = 65$ for all Bn .

greater dominance of convection effect on species transport, and thus the effect of yield stress on mixing pertaining to this case becoming different than as discussed for smaller Pe . Due to the highly convection dominated species transport, the species concentration follows the flow pattern as well for higher Pe . The higher amount of species transport from the inlet to near the cylinder and together with the presence of the vortex therein promotes the mixing of the fluid streams. In addition, the value of C_∞ also decreases in this instance due to the Bn -induced decrease in flow velocity. However, it is noteworthy that the value of C at the outlet also decreases as a result of the reduced inflow flow velocity with Bn . Due to the dominant effect of lowering the C value at the outlet with increasing Bn , $|C - C_\infty|_{\text{avg}}$ can be reduced, as evident on the right side of Fig. 7(b). As a result, we can infer that at $Pe = 500$, species homogeneity relative to C_∞ is enhanced with an increase in Bn .

The forgoing discussion is suggestive that the underlying mixing nontrivially changes owing to an intricate interplay between flow and fluid properties. Considering this aspect, we plot the variation of mixing efficiency (η) with a change in Pe is depicted in Fig. 8, obtained for different values of Bn . For all Bn , we observe that the mixing efficiency exhibits an increasing–decreasing trend with an increase in Pe . The increasing pattern in mixing efficiency is anticipated with an increase in Pe for lower Pe values up to 65. The reduction in $|C - C_\infty|_{\text{avg}}$ with Pe up to 65 can be attributed to the augmentation in species concentration homogeneity concerning C_∞ concentration. The increase in Pe values in its lower regime causes the value of C to increase from lower values toward the C_∞ at the outlet section due to the intensified convective species transport with Pe . Consequently, $|C - C_\infty|_{\text{avg}}$ decreases with Pe up to 65, resulting in an increase in mixing efficiency up to $Pe = 65$. Furthermore, the value of C at the outlet section can exceed the homogeneity concentration, C_∞ , due to the substantial increase in convective species transport strength as Pe exceeds $Pe = 65$. As a result, an increase in $|C - C_\infty|_{\text{avg}}$ with Pe for $Pe > 65$ permits a decrease in mixing efficiency with Pe . Additionally, for lower Pe values (1–8), the mixing efficiency increases as Bn increases as shown in Fig. 8. It is because Bn can reduce the value of C at the outlet due to the decrease in flow velocity. Because of the dominance of this impact, the value of $|C - C_\infty|_{\text{avg}}$ for the outlet section decreases with Bn , thereby improving the mixing efficiency within $Pe < 8$. Further, the mixing efficiency slightly declines with an increase in Bn for Pe values between 8 and 50. According to Fig. 7(a), the slight increase in $|C - C_\infty|_{\text{avg}}$ with Bn in this range of Pe is responsible for the observed effect. Finally, mixing efficiency continues to exhibit a growing pattern with Bn at larger values of Pe (50–1000). According to Fig. 7(b), it is caused by reductions in the value of

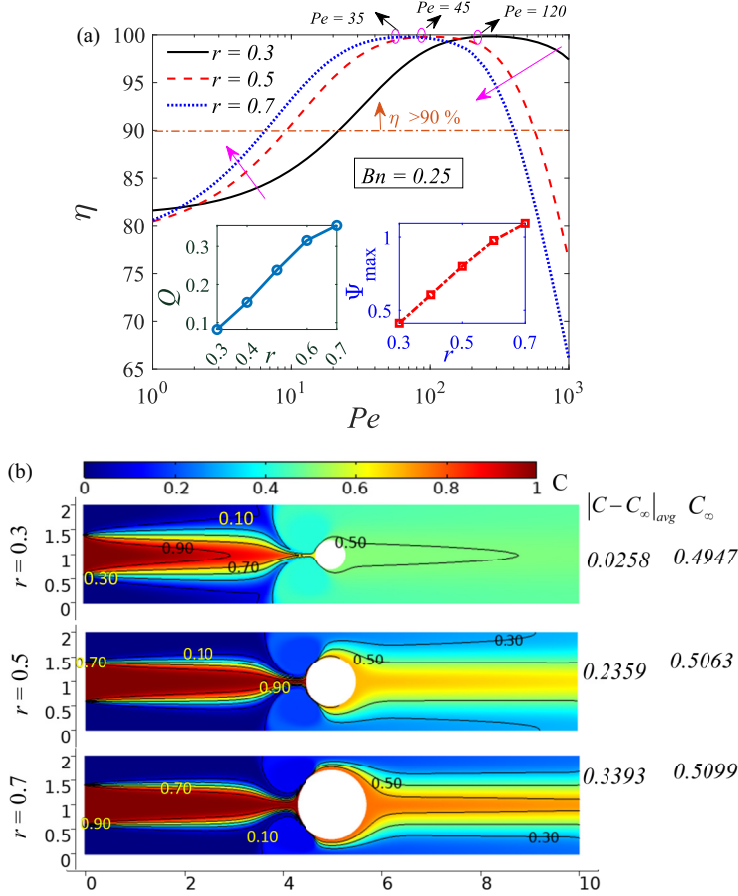


FIG. 9. (a) Variation of mixing efficiency with Pe at different r when $Bn = 0.25$ and $n = 0.5$. The variations of maximum vortex strength (Ψ_{\max}) and dimensionless flow rate (Q) with r is depicted in the inset. Also, the corresponding minimum Pelet number for which mixing efficiency approaches 99% is also indicated. (b) Contours of dimensionless species concentration contours at different r when $Pe = 1000$, $Bn = 0.25$, and $n = 0.5$. The corresponding average deviation in concentration field over the fully mixed condition ($C = C_\infty$), i.e., $|C - C_\infty|_{\text{avg}}$ is also depicted in the right side of the figure.

$|C - C_\infty|_{\text{avg}}$ for this range of Pe , which in turn improves mixing efficiency with Bn at larger values of Pe .

E. Effect of cylinder radius on mixing efficiency

In this section, the effort has been made to analyze the effect of the cylinder radius on mixing efficiency for viscoplastic fluids in the physically justified range of diffusive Pelet number. The variation of mixing efficiency with change in Pe at different r is depicted in Fig. 9(a) when $Bn = 0.25$. When Pe approaches unity, we observe that the mixing efficiency is higher for the smaller radius ($r = 0.3$). It is explained by the fact that, compared to larger radii, the weaker flow velocity at smaller radii (see Appendix C) results in smaller C values at outlet sections that are closer to the uniformity condition concentration, C_∞ . For the lower radius ($r = 0.3$) compared to the larger radii ($r = 0.5$ and 0.7), as Pe tends toward unity, there is a reduced prediction of $|C - C_\infty|_{\text{avg}}$. Therefore, when Pe approaches unity, higher mixing efficiency is obtained for a smaller radius

($r = 0.3$). Further, it is found that the mixing efficiency is enhanced with an increase in r at the intermediate values of Pe . This increase in efficiency is because of the increase in the intensity of flow velocity near the cylinder (see Fig. 5) with r . An enhancement of flow velocity with r augments the core velocity as well, which in turn allows stronger stream function strength, Ψ_{\max} [see variation of Ψ_{\max} with r in the inset of Fig. 9(a)]. With an increase in r , therefore, a greater amount of tracer fluid gets transported and mixed by the vortex of higher strength. As a result, a more uniform concentration field which is close to the uniformity concentration, C_{∞} , is obtained at higher r , and results in an enhancement of η with r . Additionally, as depicted in Fig. 9(a), it is evident that the minimal Peclet number required to achieve mixing efficiencies close to 99% follows a decreasing trend as the radius increases. This observation aligns with the fact that a larger flow rate at a larger radius transports more tracer liquid into the domain [see inset of Fig. 9(a)]. Consequently, this enables the attainment of $\eta = 99\%$ at a significantly lower value of Pe for a larger radius, resulting in a relatively lower $|C - C_{\infty}|_{\text{avg}}$. Importantly, for the intermediate Pe values, both mixing efficiency and flow rate are enhanced with r [see variation of Q with r in the inset of Fig. 9(a)]. Therefore, this is the condition of “quick and efficient mixing.” However, for the higher values of Pe , the effect of r on mixing efficiency is seen to be opposite. The higher strength of primary core flow for higher radius allows a larger amount of species to get injected into the field. This effect, as shown in Fig. 9(b), leads to a decrease of the species uniformity at the outlet owing to an increase in $|C - C_{\infty}|_{\text{avg}}$ at $Pe = 1000$ [see right side of Fig. 9(b)]. Notably, from the forgoing discussion it is seen that the smaller cylinder radius ($r = 0.3$) is beneficial for the mixing of candidate fluids having very high Pe ($\gg 1$).

F. Shear-induced binary aggregation kinetics for viscoplastic fluid

The mixing of biological fluids that contain biomolecules such as proteins and DNA is characterized by the shear-induced binary aggregation kinetics [40,51]. For two-body aggregation, let the kinetic constant for the aggregation of the primary particle be $k_{1,1}$ and its reciprocal is the characteristic time of aggregation (t_c). The mathematical expression of t_c for the shear-induced aggregation kinetics is written as [53]

$$t_c \sim \frac{\exp(-6\pi\alpha_s\mu_r^*\dot{\gamma}^*a^3/k_B T)}{\sqrt{3\pi\alpha_s\mu_r^*\dot{\gamma}^*a^3/k_B T}}. \quad (17)$$

In this context, it is important to note that in Ref. [53], the two-body Smoluchowski equation was employed with a constant shear to study binary (two-particle) aggregation. While constant shear was used to simulate the aggregation time, a closer examination of the time-dependent viscosity of charge-stabilized polystyrene colloids under different shear rate in Ref. [53] reveals that it is crucial to calculate the typical time frame of aggregation, beyond which viscosity increases almost asymptotically. Equation (17), which links shear rate, particle size, and solution viscosity to the characteristic time of two-body aggregation, can be used for this estimation. Furthermore, the time-dependent viscosity data for charge-stabilized polystyrene colloids under different shear rates in Ref. [53] indicates that higher shear rates correspond to the minimal critical time for a significant increase in viscosity due to aggregation. In this context, the “characteristic time of binary aggregation” gives an idea of the timescale beyond which a higher probability of binary aggregation results in a substantial viscosity increase, achieved by increasing the effective volume fraction of clusters through two-body hydrodynamic interactions. As a result, the present work estimates the characteristic time of binary aggregation based on the maximum shear rate. In addition, in Eq. (17), the Peclet number for the transport of particle is $Pe_c = 3\pi\mu_r^*\dot{\gamma}^*a^3/k_B T$. The ratio ($t_{\text{Diff}}/t_{\text{Con}}$) of the diffusive timescale based on particle size [$t_{\text{Diff}} = a^2/(k_B T/(3\pi\mu_r^*a))$] to the convective timescale ($t_{\text{Con}} = 1/\dot{\gamma}^*$) can be used for establishing the diffusive Peclet number associated with the particle interaction ($Pe_c = 3\pi\mu_r^*\dot{\gamma}^*a^3/k_B T$). The other parameters are taken as $T = 300$ K, $a_s = 1/3\pi$, $a = 100$ nm [40,53], and $m = 0.017$ Pa s^m [27]. The maximum Pe_c is obtained up to 12.199 for $r = 0.7$. Therefore, binary aggregation must be convection dependent. It may be mentioned here

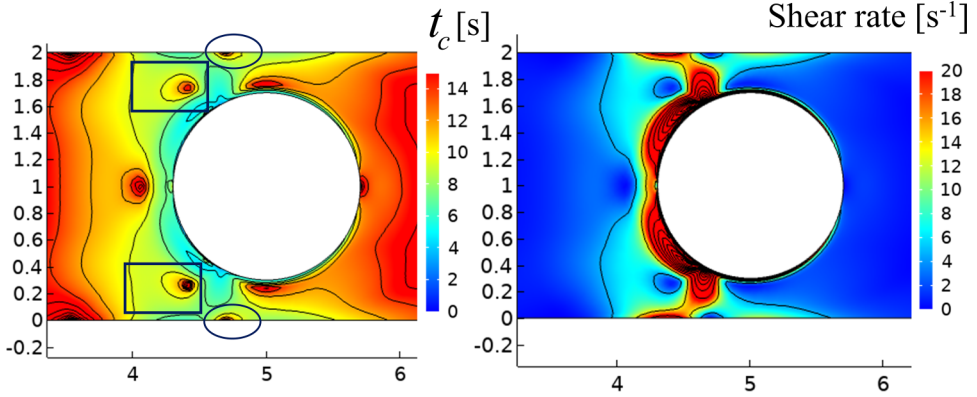


FIG. 10. Contours of characteristic time (t_c) of the binary aggregation (left) and shear rate (right) near the cylinder when $r = 0.7$, $n = 0.5$, and $Bn = 0.25$. For the calculation of t_c , the other parameters are taken as $T = 300$ K, $a_s = 1/3\pi$, $a = 100$ nm, and $m = 0.017$ Pa s n .

that the probability of collision rate of the particle is enhanced with the increase in $\dot{\gamma}^*$, while at the same time, the activation energy for the aggregation decreases with $\dot{\gamma}^*$ as well [53]. Therefore, an exponential increase in reaction rate for two-body aggregation and an exponential decrease in the kinetic constant for the aggregation with $\dot{\gamma}^*$ is predicted to visualize the binary aggregation kinetics. To see the clear visualization of t_c , the corresponding contour is depicted in Fig. 10 (left side). As seen, the intensity of t_c is much lower near the cylinder upstream side. This is because of the higher intensity of shear rate near this region (see shear rate contours on the right side of Fig. 10) due to the existence of the stronger flow velocities therein (see Fig. 5). The stagnant region at the vortex center allows a nearly zero shear rate which causes a higher intensity of t_c (see rectangular box in the left side of Fig. 10). Also, the stagnant region at the interface of the primary and secondary flow junction, formed near the top and bottom plane wall, causes a higher intensity of t_c (see elliptical box) as the intensity of shear rate is smaller therein. For other regions, the weaker shear rate causes a higher intensity of t_c .

Further, with the variation of t_c , based on the maximum shear rate, various n are depicted in Fig. 11(a) while varying the cylinder radius. The variations are shown for two values of Bn ($= 0$,

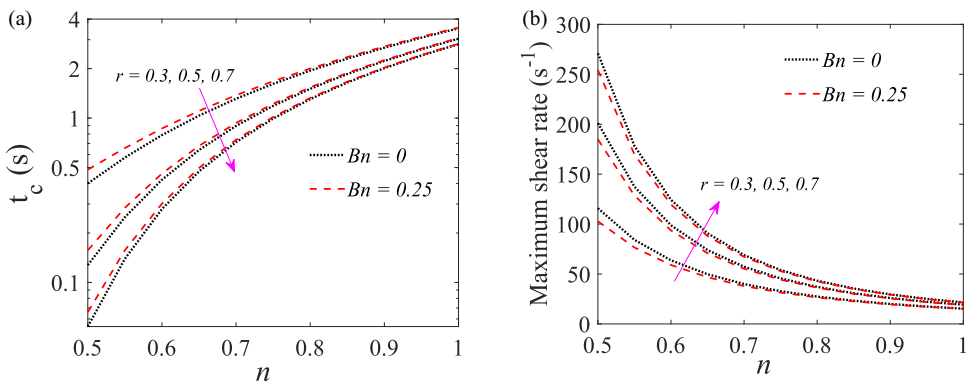


FIG. 11. (a) Variation of characteristic time (t_c) of the binary aggregation based on maximum shear rate in domain with change in fluid behavior index (n) at the different values of r and Bn . (b) Variation of maximum shear rate with fluid behavior index (n) at the different values of r and Bn . The other parameters are taken as $T = 300$ K, $a_s = 1/3\pi$, $a = 100$ nm, and $m = 0.017$ Pa s n .

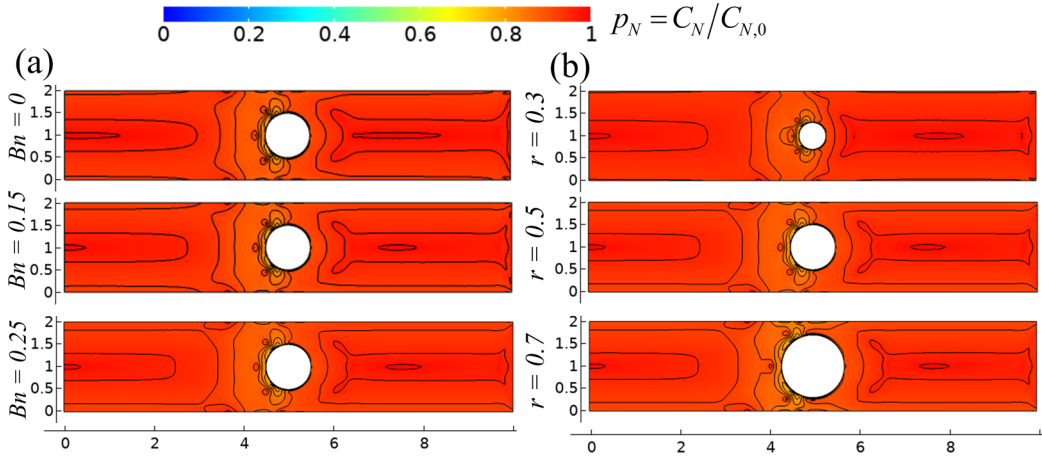


FIG. 12. (a) Contours of particle probability density distribution [$p_N = C_N/C_{N,0} = 1/(1 + t_{\text{ref}}/t_c)$] at different Bn in steady state when $r = 0.5$, $n = 0.5$, $T = 300$ K, $a_s = 1/3\pi$, $a = 100$ nm, and $m = 0.017$ Pa s n . (b) Contours of p_N at different cylinder radius in steady state when $Bn = 0.25$, $n = 0.5$, $T = 300$ K, $a_s = 1/3\pi$, $a = 100$ nm, and $m = 0.017$ Pa s n .

0.25). Interestingly, t_c is enhanced with n . The decrease in the maximum shear rate with an increase in n [see Fig. 11(b)] is mainly due to the reduction in shear-thinning behavior. This reduction leads to an enhancement of t_c [see Eq. (17)]. The relatively smaller prediction of maximum shear rate for $Bn = 0.25$ compared to $Bn = 0$ [see Fig. 11(b)] allows higher t_c . Also, the enhancement in maximum shear rate with r [see Fig. 11(b)] due to the enhancement in flow intensity (see Fig. 5) allows a decrease in t_c with r for the considered range of n .

We can correlate the associated probability density (p_N) of finding a second particle within a radius $b = 2a$ (a is the particle radius) based on the bulk number concentration of particles, $C_{N,0}$. Accordingly, the probability number concentration field (C_N) can be expressed as $C_N = C_{N,0}p_N$ [53]. Therefore, the probability density of aggregation [70,71] within the domain can also be estimated as described in $p_N = C_N/C_{0,\text{max}} = 1/(1 + t_{\text{ref}}/t_c)$ [53]. Therefore, by estimating t_c and the shear rate field, the probability density of particles aggregating can be estimated in the domain. Here, the contours of p_N are depicted in Fig. 12(a) for different values of Bn . It is observed from Fig. 12(a) that the increase in Bn enhances the thickness of maxima p_N near the upstream and downstream core regions. This observation is because of the increasing unyielded region thickness with Bn where the shear rate is nearly zero. Therefore, the smaller shear rate results in higher t_c and maximizes the probability of a higher intensity of particle number concentration. It is for this reason that p_N approaches unity in that region. Similar observations are predicted in Fig. 12(b) that an increase in cylinder radius decreases the thickness of maxima p_N due to the reduced unyielded core region near the upstream and downstream parts of the cylinder (see Fig. 6). The intensity of p_N seems to be smaller near the cylinder region except for the smaller flow stagnation regions [see Fig. 10(a)]. The higher intensity of t_c inside the flow stagnation region [see Fig. 10(a)] allows a higher intensity of p_N . Importantly, it should be noted that the proposed approach for predicting the probability density of particles aggregating in a binary fashion under shear is less expensive and simpler than the method used for estimating the actual particle number concentration field. Note that the actual particle number concentration field is typically calculated from a full-scale Lagrangian particle tracing, which is indeed computationally intensive. While quantitative estimation requires the expensive Lagrangian particle tracing method, the current approach offers a qualitative representation of the probability distribution of particle numbers in binary aggregation under shear.

V. CONCLUDING REMARKS

We have investigated electroosmotic mixing of viscoplastic fluids in a microchannel with a built-in two-part cylinder having the same sign but different zeta potential in its upstream and downstream portions. We have solved the transport equations numerically, and the underlying mixing efficiency (η) and shear-induced binary aggregation kinetics for the chosen configuration are studied systematically for a set of pertinent parameters. Effort has also been taken to benchmark the modeling framework developed here, and it has been demonstrated that results obtained from the present endeavor in the limiting cases show good agreement with the reported experimental and theoretical results.

We have shown that the flow velocity developed in the field due to in built geometry modulated EDL phenomenon upon interacted with the viscous resistance leads to the generation of vortices in the regions between the plane wall and built-in cylinder. We have shown through this analysis that both inevitable yield stress and the shear-thinning nature of viscoplastic fluid promotes the vortex generation in the field following the flow reversal phenomenon. As shown, inevitable yield stress of the viscoplastic fluid only minimally impacts the vortex generation, while the shear-thinning nature of the fluid triggers the vortex generation phenomenon substantially. Additionally, it was observed that flow velocity and flow rate increased with greater cylinder radius, but decreased as flow behavior indices and Bingham numbers increased. It has also been seen that the presence of the stagnation zone forms between the primary flow close to the walls and the recirculation zone allows for the development of smaller unyielding zones, and its size decreases as the cylinder radius increases. Quite interestingly, it is seen that at smaller cylinder radius, a ψ -shaped unyielded zone has emerged in the downstream side of the cylinder. This onset of unyielded zone, which is affected by the cylinder radius and diffusive Peclet number, nontrivially modulates the mixing efficiency of viscoplastic fluids. With an increase in the diffusive Peclet number, it was observed that mixing efficiency followed an increasing–decreasing trend. Also, at lower and higher values of the diffusive Peclet number, mixing efficiency increases with the Bingham number, although it slightly decreases with the Bingham number for intermediate values of the Peclet number. Additionally, it was found that mixing efficiency is greater for smaller radii when the diffusive Peclet number approaches unity. At intermediate diffusive Peclet numbers, it exhibits an increasing pattern with increasing cylinder radius, while at higher diffusive Peclet numbers, it decreases with radius. We have established that the condition leading to “rapid and efficient mixing” is that the flow velocity and underlying mixing efficiency both increase with an increase in the cylindrical radius. Interestingly, when the cylinder radius is lower, the proposed micromixer predicts greater than 95% mixing efficiency up to higher values of the diffusive Peclet number ($\sim 10^3$). Moreover, we have unveiled that the flow field developed near the built-in cylinder has a significant impact on the characteristic time of binary aggregation kinetics—an index that underlines the mixing of solutes and biofluids that contain colloidal particles. For viscoplastic fluids, a slightly higher value of the characteristic time for binary aggregation, based on the maximum shear rate, is observed compared to the case with zero yield stress. Furthermore, the characteristic time for binary aggregation is enhanced with an increase in the flow behavior index and reduces with an increase in the cylinder radius. Interestingly, it has been observed that the fluid yield stress has a significant influence on the predicted distribution of particle probability density distribution based on the characteristic time of binary aggregation. We believe that inferences of this endeavor may certainly be useful in designing the state-of-the-art micromixers intended for efficient mixing of viscoplastic fluids in particular, and effective solute mixing in general.

ACKNOWLEDGMENTS

P.K.M. gratefully to acknowledges the financial support provided by the SERB (DST), India, through Project No. MTR/2020/000034. The authors would like to thank the anonymous reviewers for their insightful comments and constructive suggestions to improve the quality of the paper.

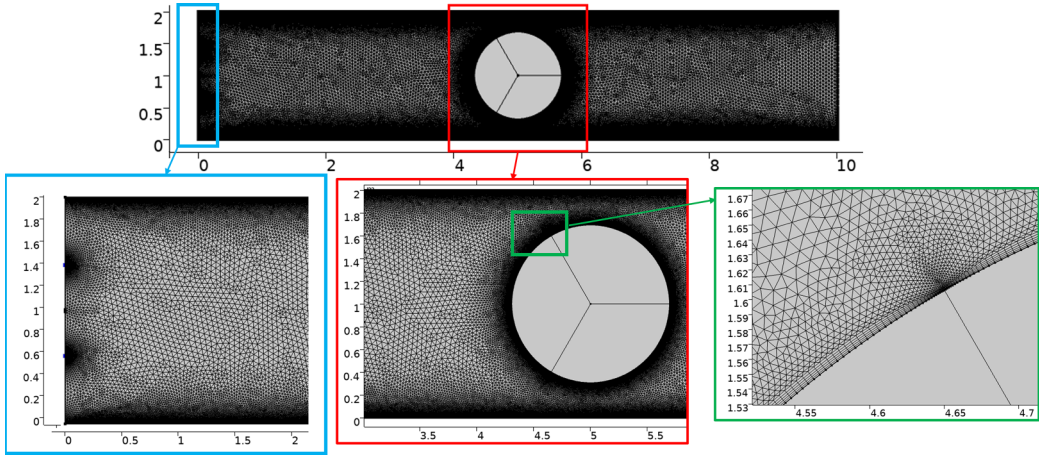


FIG. 13. Mesh structure in the domain. The denser mesh is taken near the cylinder wall to predict an accurately sharp EDL potential gradient, ψ , and velocity gradient, and comparatively denser near the region having discontinuity in the zeta potential boundary condition (see zoomed view of the mesh structure in the bottom-right part) and species concentration boundary condition discontinuity at the inlet (see zoomed view of the mesh structure in the bottom-left part). The dimensionless element size range near the cylinder wall (except the region of zeta potential and species concentration boundary condition discontinuity) and the plane wall is taken as 0.005 to 4×10^{-5} , while the same range is taken as 0.001 to 4×10^{-5} at the region having discontinuity in the zeta potential and species concentration boundary conditions.

APPENDIX A: MESH STRUCTURE IN THE DOMAIN

In this appendix, we demonstrate in Fig. 13 the mesh structure inside the domain. At the inlet where two liquids arrive the mesh structure is denser. Additionally, the closer look at the cylinder makes it evident that the denser mesh at the zeta potential discontinuity point is necessary to accurately anticipate the EDL potential gradient.

APPENDIX B: EFFECT OF STRESS GROWTH PARAMETER ON FLOW RATE AND RECIRCULATION VELOCITY

The computed solution also gets influenced by the dimensionless stress growth parameter, which was first put out by Papanastasiou and Boudouvis and controls the yield-stress's exponential growth. Table II shows the corresponding change in the dimensionless flow rate at various M_p . Additionally, Fig. 14 shows how flow rate and recirculation velocity change when M_p varies.

TABLE II. Variation of dimensionless flow rate (Q) and error in Q with respect to corresponding value at $M_p = 800$ with a change in M_p when $r = 0.7$, $n = 0.5$, and $Bn = 0.25$.

M_p	50	100	200	300	400	500	600	700	800
Q	0.35455	0.35445	0.3544	0.35437	0.35436	0.35434	0.35445	0.35445	0.35444
Percentage error in Q with respect to $M_p = 800$	3.10×10^{-2}	2.82×10^{-3}	-1.13×10^{-2}	-1.97×10^{-2}	-2.26×10^{-2}	-2.82×10^{-2}	2.82×10^{-3}	2.82×10^{-3}	

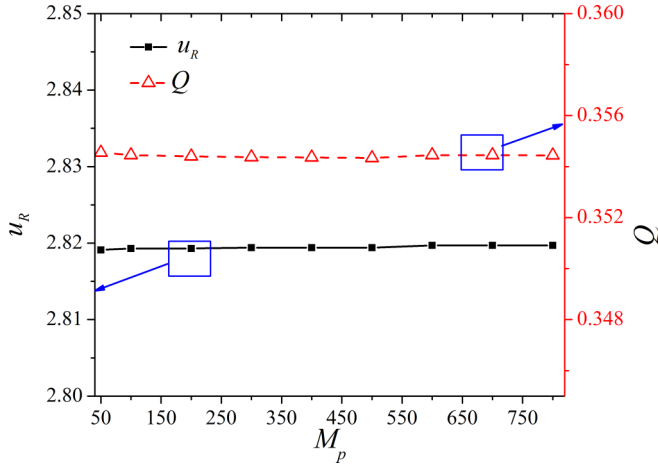


FIG. 14. Variation of Q and dimensionless recirculation velocity (u_R) with M_p when $r = 0.7$, $n = 0.5$, and $Bn = 0.25$.

APPENDIX C: EXTERNAL ELECTRIC FIELD, EQUIPOTENTIAL LINES, AND FLOW VELOCITY PROFILE AT DIFFERENT RADIUS

The influence of cylinder radius (r) on the equipotential lines and dimensionless electric field intensity is discussed in this appendix in Fig. 15. It is observed that between the cylinder and plane wall, the distance between equipotential lines is less. This is because of denser electric field lines in this location. Thus, the aforementioned region likewise has a higher electric field intensity. Additionally, when the cylinder radius is greater between the cylinder and plane wall, the distance between equipotential lines is reduced because of the denser electric field lines. The intensity of the electric field there increases with radius as a result. Furthermore, Fig. 16 shows how the cylinder radius affects the flow velocity profile.

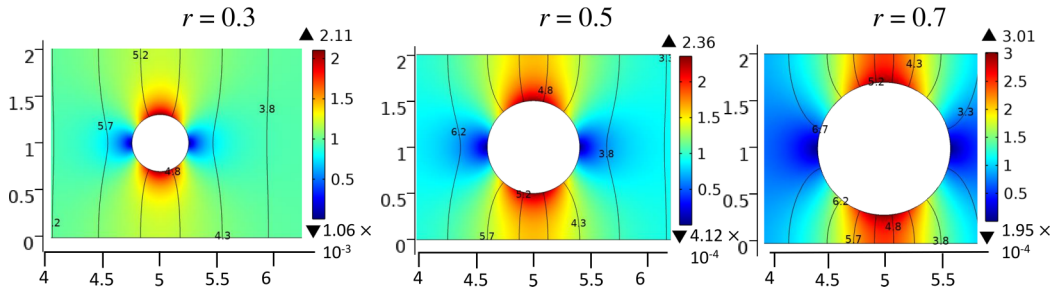


FIG. 15. Contours of dimensionless electric field intensity and equipotential lines at different cylinder radius. The legend of the dimensionless external electric field magnitude $[\sqrt{(\partial\phi/\partial x)^2 + (\partial\phi/\partial y)^2}]$ is shown in the right side of the image.

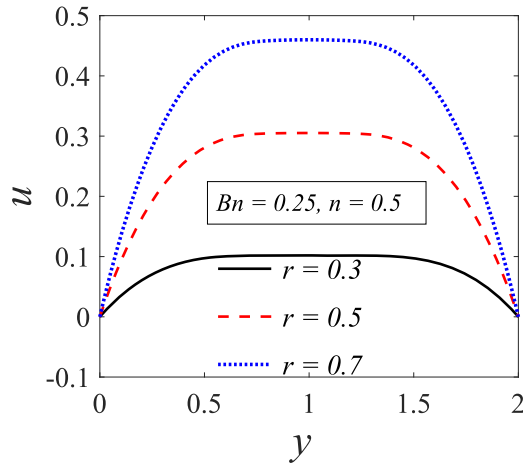


FIG. 16. Dimensionless flow velocity profile at $x = 2$ at different r when $n = 0.5$ and $Bn = 0.25$.

-
- [1] G. Li, A. Townsend, L. A. Archer, and D. L. Koch, Suppression of electroconvective and morphological instabilities by an imposed cross flow of the electrolyte, *Phys. Rev. Fluids* **6**, 033701 (2021).
- [2] M. Dietzel and S. Hardt, Electroosmotic flow in small-scale channels induced by surface-acoustic waves, *Phys. Rev. Fluids* **5**, 123702 (2020).
- [3] R. Abu-Rjal, I. Rubinstein, and B. Zaltzman, Driving factors of electro-convective instability in concentration polarization, *Phys. Rev. Fluids* **1**, 023601 (2016).
- [4] M. Mirzadeh, T. Zhou, M. A. Amooie, D. Fraggedakis, T. R. Ferguson, and M. Z. Bazant, Vortices of electro-osmotic flow in heterogeneous porous media, *Phys. Rev. Fluids* **5**, 103701 (2020).
- [5] S. Dehe, B. Rofman, M. Bercovici, and S. Hardt, Electro-osmotic flow enhancement over superhydrophobic surfaces, *Phys. Rev. Fluids* **5**, 053701 (2020).
- [6] A. Hashemi, G. H. Miller, and W. D. Ristenpart, Asymmetric rectified electric fields generate flows that can dominate induced-charge electrokinetics, *Phys. Rev. Fluids* **5**, 013702 (2020).
- [7] A. Sadeghi, M. Azari, and S. Hardt, Electroosmotic flow in soft microchannels at high grafting densities, *Phys. Rev. Fluids* **4**, 063701 (2019).
- [8] A. Gupta, B. Rallabandi, and H. A. Stone, Diffusiophoretic and diffusioosmotic velocities for mixtures of valence-asymmetric electrolytes, *Phys. Rev. Fluids* **4**, 043702 (2019).
- [9] A. Morozov, D. Marenduzzo, and R. G. Larson, Hydrodynamic bifurcation in electro-osmotically driven periodic flows, *Phys. Rev. Fluids* **3**, 063702 (2018).
- [10] U. Ghosh, S. Mandal, and S. Chakraborty, Electroosmosis over charge-modulated surfaces with finite electrical double layer thicknesses: Asymptotic and numerical investigations, *Phys. Rev. Fluids* **2**, 064203 (2017).
- [11] H. Feng, T. N. Wong, and Z. Che, Induced charge electrophoresis of a conducting cylinder in a nonconducting cylindrical pore and its micromotoring application, *Phys. Rev. Fluids* **1**, 044103 (2016).
- [12] R. Riahi, A. Tamayol, S. A. M. Shaegh, A. M. Ghaemmaghami, M. R. Dokmeci, and A. Khademhosseini, Microfluidics for advanced drug delivery systems, *Curr. Opin. Chem. Eng.* **7**, 101 (2015).
- [13] B. Ziaie, A. Baldi, M. Lei, Y. Gu, and R. A. Siegel, Hard and soft micromachining for BioMEMS: Review of techniques and examples of applications in microfluidics and drug delivery, *Adv. Drug Delivery Rev.* **56**, 145 (2004).

- [14] O. Y. F. Henry and C. K. O'Sullivan, Rapid DNA hybridization in microfluidics, *TrAC Trends Anal. Chem.* **33**, 9 (2012).
- [15] X. Weng, H. Jiang, and D. Li, Microfluidic DNA hybridization assays, *Microfluid. Nanofluid.* **11**, 367 (2011).
- [16] A. A. S. Bhagat, H. Bow, H. W. Hou, S. J. Tan, J. Han, and C. T. Lim, Microfluidics for cell separation, *Med. Biol. Eng. Comput.* **48**, 999 (2010).
- [17] T. Salafi, K. K. Zeming, and Y. Zhang, Advancements in microfluidics for nanoparticle separation, *Lab Chip* **17**, 11 (2017).
- [18] L. Capretto, W. Cheng, M. Hill, and X. Zhang, *Micromixing Within Microfluidic Devices BT - Microfluidics: Technologies and Applications*, edited by B. Lin (Springer, Berlin, Heidelberg, 2011), pp. 27–68.
- [19] Z. Yang, S. Matsumoto, H. Goto, M. Matsumoto, and R. Maeda, Ultrasonic micromixer for microfluidic systems, *Sens. Actuators, A* **93**, 266 (2001).
- [20] D. Gao, F. Jin, M. Zhou, and Y. Jiang, Recent advances in single cell manipulation and biochemical analysis on microfluidics, *Analyst* **144**, 766 (2019).
- [21] Z. Li, Q. Bao, C. Liu, Y. Li, Y. Yang, and M. Liu, Recent advances in microfluidics-based BioNMR analysis, *Lab Chip* **23**, 1213 (2023).
- [22] N. Sun and D. De Kee, Simple shear, hysteresis and yield stress in biofluids, *Can. J. Chem. Eng.* **79**, 36 (2001).
- [23] F. J. Walburn and D. J. Schneck, A constitutive equation for whole human blood, *Biorheology* **13**, 201 (1976).
- [24] A. J. Apostolidis, M. J. Armstrong, and A. N. Beris, Modeling of human blood rheology in transient shear flows, *J. Rheol.* **59**, 275 (2015).
- [25] A. L. Cheng, N. M. Pahlevan, D. G. Rinderknecht, J. C. Wood, and M. Gharib, Experimental investigation of the effect of non-newtonian behavior of blood flow in the Fontan circulation, *Eur. J. Mech., B: Fluids* **68**, 184 (2018).
- [26] A. J. Apostolidis and A. N. Beris, Modeling of the blood rheology in steady-state shear flows, *J. Rheol.* **58**, 607 (2014).
- [27] S. S. Shibeshi and W. E. Collins, The rheology of blood flow in a branched arterial system, *Appl. Rheol.* **15**, 398 (2005).
- [28] N. Bag and S. Bhattacharyya, Electroosmotic flow of a non-Newtonian fluid in a microchannel with heterogeneous surface potential, *J. Non-Newtonian Fluid Mech.* **259**, 48 (2018).
- [29] S. Bhattacharyya and D. Kundu, Enhanced electroosmotic flow, conductance and ion selectivity of a viscoplastic fluid in a hydrophobic cylindrical pore, *Appl. Math. Model.* **111**, 802 (2022).
- [30] C. O. Ng and C. Qi, Electroosmotic flow of a viscoplastic material through a slit channel with walls of arbitrary zeta potential, *Phys. Fluids* **25**, 103102 (2013).
- [31] M. Patel, S. S. H. Kruthiventi, and P. Kaushik, Polyelectrolyte layer grafting effect on the rotational electroosmotic flow of viscoplastic material, *Microfluid. Nanofluid.* **25**, 1 (2021).
- [32] C. Qi and C. O. Ng, Rotating electroosmotic flow of viscoplastic material between two parallel plates, *Colloids Surf., A* **513**, 355 (2017).
- [33] S. Bhattacharyya and N. Bag, Enhanced electroosmotic flow of Herschel-Bulkley fluid in a channel patterned with periodically arranged slipping surfaces, *Phys. Fluids* **31**, 072007 (2019).
- [34] B. Rallabandi, C. Wang, and S. Hilgenfeldt, Analysis of optimal mixing in open-flow mixers with time-modulated vortex arrays, *Phys. Rev. Fluids* **2**, 064501 (2017).
- [35] F. Khalkhal and S. Muller, Analyzing flow behavior of shear-thinning fluids in a planar abrupt contraction/expansion microfluidic geometry, *Phys. Rev. Fluids* **7**, 023303 (2022).
- [36] J. E. Dick, C. Renault, and A. J. Bard, Observation of single-protein and DNA macromolecule collisions on ultramicroelectrodes, *J. Am. Chem. Soc.* **137**, 8376 (2015).
- [37] N. Rawat and P. Biswas, Size, shape, and flexibility of proteins and DNA, *J. Chem. Phys.* **131**, 165104 (2009).
- [38] L. Costigliola, D. M. Heyes, T. B. Schröder, and J. C. Dyre, Revisiting the Stokes-Einstein relation without a hydrodynamic diameter, *J. Chem. Phys.* **150**, 021101 (2019).

- [39] E. Biddiss, D. Erickson, and D. Li, Heterogeneous surface charge enhanced micromixing for electrokinetic flows, *Anal. Chem.* **76**, 3208 (2004).
- [40] H. S. Gaikwad, G. Kumar, and P. K. Mondal, Efficient electroosmotic mixing in a narrow-fluidic channel: The role of a patterned soft layer, *Soft Matter* **16**, 6304 (2020).
- [41] K. N. Vasista, S. K. Mehta, and S. Pati, Electroosmotic mixing in a microchannel with heterogeneous slip dependent zeta potential, *Chem. Eng. Process.* **176**, 108940 (2022).
- [42] S. K. Mehta and S. Pati, Enhanced electroosmotic mixing in a wavy micromixer using surface charge heterogeneity, *Ind. Eng. Chem. Res.* **61**, 2904 (2022).
- [43] S. K. Mehta, S. Pati, and P. K. Mondal, Numerical study of the vortex-induced electroosmotic mixing of non-Newtonian biofluids in a nonuniformly charged wavy microchannel: Effect of finite ion size, *Electrophoresis* **42**, 2498 (2021).
- [44] B. Mahapatra and A. Bandopadhyay, Efficacy of microconfined fluid mixing in a combined electroosmotic and pressure driven transport of complex fluid over discrete electrodes, *Phys. Fluids* **34**, 042012 (2022).
- [45] D. Pandey, P. K. Mondal, and S. Wongwises, Dielectric polarization mediated efficient solute mixing: Effect of the geometrical configuration of polarizing blocks, *Electrophoresis* **44**, 1637 (2023).
- [46] L. Mei, D. Cui, J. Shen, D. Dutta, W. Brown, L. Zhang, and I. K. Dabipi, Electroosmotic mixing of non-Newtonian fluid in a microchannel with obstacles and zeta potential heterogeneity, *Micromachines* **12**, 431 (2021).
- [47] M. Alipanah, M. Hatami, and A. Ramiar, Thermal and rheological investigation of non-Newtonian fluids in an induced-charge electroosmotic micromixer, *Eur. J. Mech., B: Fluids* **88**, 178 (2021).
- [48] S. Shyam, P. K. Mondal, and B. Mehta, Magnetofluidic mixing of a ferrofluid droplet under the influence of time-dependent external field, *J. Fluid Mech.* **917**, A15 (2021).
- [49] M. Hadigol, R. Nosrati, A. Nourbakhsh, and M. Raisee, Numerical study of electroosmotic micromixing of non-Newtonian fluids, *J. Non-Newtonian Fluid Mech.* **166**, 965 (2011).
- [50] A. Banerjee and A. K. Nayak, Influence of varying zeta potential on non-Newtonian flow mixing in a wavy patterned microchannel, *J. Non-Newtonian Fluid Mech.* **269**, 17 (2019).
- [51] S. K. Mehta and P. K. Mondal, Vortex-assisted electroosmotic mixing of Carreau fluid in a microchannel, *Electrophoresis* **44**, 1629 (2023).
- [52] C. Wang, Y. Song, and X. Pan, Electrokinetic-vortex formation near a two-part cylinder with same-sign zeta potentials in a straight microchannel, *Electrophoresis* **41**, 793 (2020).
- [53] A. Zaccone, H. Wu, D. Gentili, and M. Morbidelli, Theory of activated-rate processes under shear with application to shear-induced aggregation of colloids, *Phys. Rev. E* **80**, 051404 (2009).
- [54] T. Lorenzo and L. Marco, Brownian dynamics simulations of shear-induced aggregation of charged colloidal particles in the presence of hydrodynamic interactions, *J. Colloid Interface Sci.* **624**, 637 (2022).
- [55] L. Turetta and M. Lattuada, The role of hydrodynamic interactions on the aggregation kinetics of sedimenting colloidal particles, *Soft Matter* **18**, 1715 (2022).
- [56] S. Krishnamurthy, S. Sudhakar, and E. Mani, Kinetics of aggregation of amyloid β under different shearing conditions: Experimental and modelling analyses, *Colloids Surf., B* **209**, 112156 (2022).
- [57] Z. Xiong, Y. Cao, W.-J. Jiang, L. Zu, Q. Liang, and D. Li, Shearing induced ordered structures in two-dimensional nanomaterials-based electrodes for boosted pseudocapacitive kinetics, *Energy Storage Mater.* **53**, 444 (2022).
- [58] G. Y. Tang, C. Yang, C. K. Chai, and H. Q. Gong, Numerical analysis of the thermal effect on electroosmotic flow and electrokinetic mass transport in microchannels, *Anal. Chim. Acta* **507**, 27 (2004).
- [59] G. Y. Tang, C. Yang, J. C. Chai, and H. Q. Gong, Joule heating effect on electroosmotic flow and mass species transport in a microcapillary, *Int. J. Heat Mass Transfer* **47**, 215 (2004).
- [60] T. C. Papanastasiou and A. G. Boudouvis, Flows of viscoplastic materials: Models and computations, *Comput. Struct.* **64**, 677 (1997).
- [61] T. C. Papanastasiou, Flows of materials with yield, *J. Rheol. (Melville, NY, US)* **31**, 385 (1987).
- [62] M. V. Jafari, P. Broumand, and N. Khalili, An extended finite element method implementation in COM-

- SOL Multiphysics: Thermo-hydro-mechanical modeling of fluid flow in discontinuous porous media, *Comput. Geotech.* **159**, 105458 (2023).
- [63] A. Jafari, P. Broumand, M. Vahab, and N. Khalili, An extended finite element method implementation in COMSOL Multiphysics: Solid mechanics, *Finite Elem. Anal. Des.* **202**, 103707 (2022).
- [64] M. F. N. Mohsen, Some details of the Galerkin finite element method, *Appl. Math. Model.* **6**, 165 (1982).
- [65] Y. Huang, J. Chen, T. Wong, and J.-L. Liow, Experimental and theoretical investigations of non-Newtonian electro-osmotic driven flow in rectangular microchannels, *Soft Matter* **12**, 6206 (2016).
- [66] Y. Song, C. Wang, J. Li, and D. Li, Vortex generation in electroosmotic flow in a straight polydimethylsiloxane microchannel with different polybrene modified-to-unmodified section length ratios, *Microfluid. Nanofluid.* **23**, 24 (2019).
- [67] H. Dakhil, S. K. Basu, S. Steiner, Y. Gerlach, A. Soller, S. Pan, N. Germann, M. Leidenberger, B. Kappes, and A. Wierschem, Buffered λ -DNA solutions at high shear rates, *J. Rheol.* **65**, 159 (2021).
- [68] N. Srivastava and M. A. Burns, Analysis of non-Newtonian liquids using a microfluidic capillary viscometer, *Anal. Chem.* **78**, 1690 (2006).
- [69] R. Mehri, C. Mavriplis, and M. Fenech, Red blood cell aggregates and their effect on non-Newtonian blood viscosity at low hematocrit in a two-fluid low shear rate microfluidic dystem, *PLoS One* **13**, e0199911 (2018).
- [70] J. Bergenholtz, J. F. Brady, and M. Vacic, The non-Newtonian rheology of dilute colloidal suspensions, *J. Fluid Mech.* **456**, 239 (2002).
- [71] J. K. G. Dhont, On the distortion of the static structure factor of colloidal fluids in shear flow, *J. Fluid Mech.* **204**, 421 (1989).